THE JOURNAL OF BIOLOGICAL CHEMISTRY VOL. 288, NO. 30, pp. 21861–21875, July 26, 2013

Lack of Oncostatin M Receptor β Leads to Adipose Tissue Inflammation and Insulin Resistance by Switching Macrophage Phenotype*

Received for publication, February 14, 2013, and in revised form, June 7, 2013 Published, JBC Papers in Press, June 11, 2013, DOI 10.1074/jbc.M113.461905

Tadasuke Komori[‡], **Minoru Tanaka**[§], **Emiko Senba**[‡], **Atsushi Miyajima**[§], **and Yoshihiro Morikawa**[‡1]

From the [‡]*Department of Anatomy and Neurobiology, Wakayama Medical University, Wakayama 641-8509, Japan and the* [§]*Laboratory of Cell Growth and Differentiation, Institute of Molecular and Cellular Biosciences, The University of Tokyo, Tokyo 113-0032, Japan*

Background: OSM, a member of IL-6 family of cytokines, is involved in many inflammatory diseases.
Results: OSMRβ$^{-/-}$ mice exhibited phenotypic changes in ATMs to M1, increased proinflammatory cytokines in the adipose tissue, and systemic insulin resistance.
Conclusion: OSMRβ$^{-/-}$ mice exhibited adipose tissue inflammation and insulin resistance preceding obesity.
Significance: OSMRβ$^{-/-}$ mice constitute a unique mouse model of metabolic disorders.

Oncostatin M (OSM), a member of the IL-6 family of cytokines, plays important roles in a variety of biological functions, including inflammatory responses. However, the roles of OSM in metabolic diseases are unknown. We herein analyzed the metabolic parameters of OSM receptor β subunit-deficient (OSMRβ$^{-/-}$) mice under normal diet conditions. At 32 weeks of age, OSMRβ$^{-/-}$ mice exhibited mature-onset obesity, severer hepatic steatosis, and insulin resistance. Surprisingly, insulin resistance without obesity was observed in OSMRβ$^{-/-}$ mice at 16 weeks of age, suggesting that insulin resistance precedes obesity in OSMRβ$^{-/-}$ mice. Both OSM and OSMRβ were expressed strongly in the adipose tissue and little in some other metabolic organs, including the liver and skeletal muscle. In addition, OSMRβ is mainly expressed in the adipose tissue macrophages (ATMs) but not in adipocytes. In OSMRβ$^{-/-}$ mice, the ATMs were polarized to M1 phenotypes with the augmentation of adipose tissue inflammation. Treatment of OSMRβ$^{-/-}$ mice with an anti-inflammatory agent, sodium salicylate, improved insulin resistance. In addition, the stimulation of a macrophage cell line, RAW264.7, and peritoneal exudate macrophages with OSM resulted in the increased expression of M2 markers, IL-10, arginase-1, and CD206. Furthermore, treatment of C57BL/6J mice with OSM increased insulin sensitivity and polarized the phenotypes of ATMs to M2. Thus, OSM suppresses the development of insulin resistance at least in part through the polarization of the macrophage phenotypes to M2, and OSMRβ$^{-/-}$ mice provide a unique mouse model of metabolic diseases.

Obesity is a major factor underlying the development of insulin resistance, which is associated with a number of metabolic disorders, including type 2 diabetes, hypertension, and hyperlipidemia (1). Several lines of evidence now converge on the notion that obesity causes low-grade chronic inflammation characterized by the recruitment of macrophages, T-cells, and neutrophils into the adipose tissue (2–5). Among such inflammatory cells, the increase in adipose tissue macrophages (ATMs)[2] is associated with a further deterioration of adipose tissue inflammation and insulin sensitivity (6, 7). In contrast, a decrease in ATMs in obese mice correlates with the amelioration of adipose tissue inflammation and insulin resistance (8, 9). Therefore, ATMs play important roles in the development of the adipose tissue inflammation and insulin resistance associated with obesity.

Macrophages are a heterogeneous cell population and change their physiology in response to various microenvironmental signals. "Classically activated (M1)" macrophages are induced by two signals, IFN-γ and LPS or TNF (10). On the other hand, "alternatively activated (M2)" macrophages are induced by anti-inflammatory cytokines, such as IL-4 and IL-13 (11). In addition, M1 macrophages produce high levels of toxic intermediates (*e.g.* nitric oxide and reactive oxygen intermediates) via the activation of inducible nitric oxide synthase (iNOS) (12), whereas arginase production is increased in M2 macrophages (13).

It has recently been suggested that a high fat diet triggers the recruitment of M1 macrophages into the adipose tissue, whereas adipose tissue macrophages in lean animals exhibit an M2 phenotype (14). In obese mice, TNF-α, a potent proinflammatory cytokine, is produced by M1 ATMs (7, 15) and directly induces insulin resistance by inhibiting the insulin signaling and insulin-stimulated glucose transport, mainly in the skeletal muscle and white adipose tissue (16, 17). In contrast, M2 ATMs

* This work was supported in part by a Research Grant on Priority Areas from Wakayama Medical University and the 2012 Wakayama Medical Award for Young Researchers.

[1] To whom correspondence should be addressed: Dept. of Anatomy and Neurobiology, Wakayama Medical University, 811-1 Kimiidera, Wakayama 641-8509, Japan. Tel. and Fax: 81-73-441-0617; E-mail: yoshim@wakayama-med.ac.jp.

[2] The abbreviations used are: ATM, adipose tissue macrophage; ANOVA, analysis of variance; CREB, cAMP response element-binding protein; iNOS, nitric oxide synthase; ipGTT, intraperitoneal glucose tolerance test; ITT, insulin tolerance test; MCP, monocyte chemoattractant protein; MGL, macrophage galactose-type C-type lectin; OSM, oncostatin M; OSMRβ, OSM-specific β subunit; OSMRβ$^{-/-}$, OSMRβ-deficient; PE, phycoerythrin; PEM, peritoneal exudate macrophage; RT, room temperature; SVF, stromal vascular fraction.

secrete an anti-inflammatory cytokine, IL-10 (15). The administration of IL-10 in diet-induced obese mice enhances the activation of insulin signaling and insulin-stimulated glucose uptake in the skeletal muscle (18). Thus, the balance between M1/M2 ATMs is important for maintaining the proper balance of pro-/anti-inflammatory cytokine production in the adipose tissue, and its imbalance can lead to the development of insulin resistance. However, the mechanisms underlying the determination of the ATM phenotypes are not fully understood.

Oncostatin M (OSM), a member of the IL-6 family of cytokines, exhibits a variety of biological effects depending on the target cells by binding to a heterodimeric membrane receptor comprising the OSM-specific β subunit (OSMRβ) and gp130 (19). OSM is synthesized by various inflammatory cells, such as activated T-cells, neutrophils, eosinophils, and macrophages (20, 21). In addition, the expression of OSMRβ is induced in human peripheral blood monocytes treated with LPS (22), suggesting that OSM plays an important role in monocyte/macrophage lineage cells during inflammation. However, the roles of OSM in ATMs and in metabolic disorders remain to be elucidated. In the present study we have addressed this question using OSMRβ-deficient ($OSMR\beta^{-/-}$) mice.

EXPERIMENTAL PROCEDURES

Animals—Male C57BL/6J mice (8 weeks old) were purchased from Nihon SLC (Hamamatsu, Japan). The generation of $OSMR\beta^{-/-}$ mice has been described previously (23). $OSMR\beta^{+/+}$ wild-type (WT) and $OSMR\beta^{-/-}$ littermates were obtained from our breeding colony using heterozygous (+/−) breeding pairs. Male and female WT and $OSMR\beta^{-/-}$ mice from 8 to 32 weeks old were used in the present study. All mice were housed in specific pathogen-free facilities and under light (12 h light/dark cycle)-, temperature (22–25 °C)-, and humidity (50–60% relative humidity)-controlled conditions. Mice were allowed free access to food (MF; Oriental Yeast, Tokyo, Japan) and water.

Injection of OSM in C57BL/6J Mice—C57BL/6J mice were injected intraperitoneally with either vehicle or recombinant mouse OSM (12.5 ng/g body weight; R & D Systems, Minneapolis, MN) twice a day (10:00 and 18:00 h) for 1 week.

Injection of Sodium Salicylate in $OSMR\beta^{-/-}$ Mice—$OSMR\beta^{-/-}$ mice were injected intraperitoneally with either vehicle or sodium salicylate (120 μg/g body weight; Sigma) once a day (18:00 h) for 2 weeks.

Isolation of the Adipocyte Fraction and the Stromal Vascular Fraction (SVF)—The mice were deeply anesthetized with diethyl ether, and the epididymal adipose tissue were quickly removed. The adipose tissue was minced into fine pieces and digested with collagenase type 2 (Sigma) with PBS supplemented with 2% FCS at 37 °C for 20 min with high speed shaking. Next, the samples were passed through a 100-μm mesh (BD Biosciences) and fractioned by brief centrifugation (1200 rpm) at room temperature (RT) for 5 min. The floating cells were collected as the adipocyte fraction, and the pellets were collected as the SVF. The cells in the SVF were incubated with ammonium chloride buffer (PharmLyse; BD Biosciences) to lyse the erythrocytes.

Insulin Signaling Analysis—To evaluate insulin signaling, mice fasted for 24 h were intraperitoneally injected with human insulin (10 milliunits/g body weight). Ten minutes later epididymal fat, gastrocnemius muscle, and liver tissue were excised and frozen in liquid nitrogen. Tissue lysates were prepared as described below.

Preparation of Peritoneal Exudate Macrophages (PEMs)—The preparation of PEMs was performed as described previously with some modifications (24). Macrophages elicited in the 3 days after an intraperitoneal injection of 3 ml of thioglycollate medium (BD Biosciences) were harvested by flushing of the peritoneal cavity with Hanks' balanced salt solution (Invitrogen) with plastic syringes, suspended in DMEM (Invitrogen) with 10% FCS, and incubated on 35-mm plastic dishes for 2 h at a density of 1×10^6 cells/dish. Non-adherent cells were discarded, and the adherent cells were cultured at 37 °C for 3 days.

Treatment of PEMs with OSM—PEMs were starved in DMEM with 0.75% bovine serum albumin for 16 h before the stimulation. Then PEMs were treated with PBS or 100 ng/ml concentrations of recombinant mouse OSM and maintained for the appropriate periods.

Cell Culture—Cell culture was performed with some modifications as described previously (25). The mouse macrophage cell line, RAW 264.7, was grown in DMEM (Invitrogen) with 10% FCS, 100 units/ml of penicillin (Invitrogen), and 100 μg/ml of streptomycin (Invitrogen). All cells were grown at 37 °C in a humidified atmosphere of 5% CO_2.

Treatment of LPS and OSM for RAW 264.7 Macrophages—RAW 264.7 macrophages were plated in 35-mm dishes at a density of 1×10^6 cells/dish and cultured in a standard medium for 24 h. The cells were then treated with 10 ng/ml lipopolysaccharide (Sigma) for 16 h and washed by a standard medium twice. Then the cells were treated with vehicle or 100 ng/ml recombinant mouse OSM and maintained for 24 h.

Flow Cytometry—The cells in the SVF were incubated with anti-CD16/CD32 antibodies (1:100, BD Biosciences) to block Fc binding at 4 °C for 20 min followed by incubation with fluorescently labeled primary antibodies or control IgG at 4 °C for 30 min. The FITC-conjugated anti-F4/80, FITC-conjugated rat IgG2a isotype controls, phycoerythrin (PE)-conjugated anti-CD11c, PE-conjugated Armenian hamster IgG2a isotype controls, FITC-conjugated anti-Gr-1, FITC-conjugated rat IgG2b isotype controls, PE-conjugated anti-CD11b, and PE-conjugated rat IgG2b isotype controls were purchased from eBiosciences (San Diego, CA). The PE- or Alexa Fluor 647-conjugated anti-CD206 and their isotype controls were purchased from AbD Serotec (Oxford, UK). To detect OSMRβ in the SVF and PEMs, cells were incubated with goat anti-OSMRβ antibodies (diluted at 1: 5, R&D Systems) or control goat IgG (Jackson ImmunoResearch, West Grove, PA) at 4 °C for 30 min. Then the cells were incubated with PE-conjugated donkey anti-goat IgG (diluted at 1: 20, R&D Systems). The stained cells were analyzed using the C6 flow cytometer (BD Biosciences) or the FACSCalibur flow cytometer (BD Biosciences). Dead cells were removed from the analysis using propidium iodide staining. The flow cytometry results were analyzed using the CFlow (BD Biosciences), the CellQuest software program (BD Biosciences), or FlowJo software suites (Tree Star, Ashland, OR). The

events were first gated based on forward scatter *versus* propidium iodide to identify individual live cells. The plot of a forward *versus* side scatter was used as the second gate to gate out aggregates and debris. Next, the F4/80-positive cells were selected. Single color controls were used to set the compensation and gates.

Western Blot Analysis—Western blot analysis was performed with some modifications as described previously (25). Lysates were prepared by using radioimmune precipitation assay buffer (Upstate Biotechnology, Lake Placid, NY) containing protease inhibitor mixture (Upstate Biotechnology), 1 mM orthovanadate, 1 mM sodium fluoride, and 1 mM phenylmethylsulfonyl fluoride. The protein concentrations in the lysates were determined by using a BCA Protein Assay kit (Pierce). Twenty micrograms of protein from the samples were separated by SDS-PAGE and transferred to PVDF membranes (GE Healthcare). The blotted membranes were incubated with rat anti-CD206 antibody (diluted at 1:500, AbD Serotec), rabbit anti-CD163 antibody (diluted at 1:500, Santa Cruz Biotechnology, Santa Cruz, CA), rabbit anti-iNOS antibody (diluted at 1:500, Abcam, Cambridge, UK), mouse anti-arginase-1 antibody (BD Biosciences), rabbit anti-phosphorylated Akt antibody (diluted at 1:1000, Cell Signaling Technology, Beverly, MA), rabbit anti-Akt antibody (diluted at 1:1000, Cell Signaling Technology), rabbit anti-phosphorylated STAT3 antibody (diluted at 1:1000, Cell Signaling Technology), rabbit anti-STAT3 antibody (diluted at 1:1000, Cell Signaling Technology), rabbit anti-phosphorylated cAMP response element-binding protein (CREB) antibody (diluted at 1:1000, Cell Signaling Technology), and rabbit anti-CREB antibody (diluted at 1:1000, Cell Signaling Technology). Then the membranes were incubated with HRP-conjugated donkey anti-goat (diluted at 1:4,000, GE Healthcare), donkey anti-rat (diluted at 1:10,000, Jackson ImmunoResearch), donkey anti-rabbit (diluted at 1:20,000, GE Healthcare), or donkey anti-mouse (diluted at 1:20,000, GE Healthcare) IgG antibodies. Labeled proteins were detected with chemiluminescence using ECL detection reagent (GE Healthcare) according to the manufacturer's instructions. The membranes were exposed to hyperfilm ECL (GE Healthcare) for an appropriate period. The blotted membranes were stripped in 0.25 M glycine, pH 2.5, at RT for 10 min and incubated with rat anti-tubulin antibody (diluted at 1:500; Abcam) at 4 °C for 16 h followed by the incubation with HRP-conjugated donkey anti-rat antibody (diluted at 1:4000) at RT for 1 h.

Immunohistochemistry—Immunofluorescence staining was performed with some modifications as described previously (26, 27). Briefly, mice were deeply anesthetized with diethyl ether, and the epididymal fat pads were quickly removed. Then the fat pads were fixed with 1% paraformaldehyde in PBS at 4 °C for 1 h followed by the preincubation in 5% normal donkey serum at RT for 1 h. Then the fat pads were incubated with goat anti-OSM antibody (diluted at 1:400), goat anti-OSMRβ antibody (diluted at 1:400), rat anti-F4/80 antibody (diluted at 1:1000; AbD Serotec), and rabbit anti-caveolin-1 antibody (diluted at 1:400; BD Biosciences). The fat pads were incubated with Cy2-conjugated, Cy3-conjugated, or biotinylated secondary antibodies (diluted at 1:800; Jackson ImmunoResearch) at RT for 1 h. Then the fat pads were incubated with 7-amino-4-methylcoumarin-3-acetic acid-conjugated streptavidin (diluted at 1:500; Jackson ImmunoResearch) at RT for 30 min and mounted in the mounting media (90% glycerol and 10% PBS) on the chambered slide. Immunofluorescence images were acquired using a confocal laser scanning microscope (LSM700; Carl Zeiss, Tokyo, Japan).

To complete an immunohistochemical analysis in pancreas, mice were deeply anesthetized with diethyl ether and transcardially perfused with ice-cold 0.85% NaCl followed by ice-cold Zamboni's fixative (2% paraformaldehyde and 0.2% picric acid in 0.1 M PBS). Tissues were quickly removed, postfixed in the same fixative at 4 °C for 3 h, and cryoprotected in 20% sucrose in 0.1 M PBS. All specimens were frozen rapidly in cold *n*-hexane on dry ice and stored at −80 °C. Frozen sections were cut on a cryostat (6-μm thickness). The sections were preincubated in 5% normal donkey serum at RT for 1 h followed by the incubation with rabbit anti-insulin antibody (diluted at 1:400; Abcam). Then they were incubated with biotinylated donkey anti-rabbit IgG antibody (diluted at 1:800; Jackson ImmunoResearch) at RT for 1 h followed by incubation with HRP-conjugated streptavidin (DAKO, Carpinteria, CA) at RT for 30 min. Thereafter, the peroxidase reaction product was visualized with 0.05% diaminobenzidine tetrahydrochloride (Sigma) and 0.01% H_2O_2. After the reaction, the sections were counterstained with Eosin Y (Muto Pure Chemical, Tokyo, Japan). Images were acquired by using a BIOREVO BZ-9000 microscope (KEYENCE, Osaka, Japan). To evaluate the area of β-cell in pancreas, every 20th section was selected from a series of consecutive pancreatic sections (6 μm), and 12 sections per mouse were used for analysis. For each section the cells were considered to be positive for insulin if the cell bodies were stained brown. The area of β-cells and pancreas was measured by using Image J analysis software (Version 1.46r, Scion, Frederick, MD).

The following controls were performed: (i) incubation with protein A-purified goat or rabbit IgG instead of primary antibody; (ii) incubation without the primary antibody or without primary and secondary antibodies. None of the controls revealed any labeling (data not shown).

Measurement of Blood Glucose and Serum Insulin—These procedures were performed with some modifications as described previously (28). Mice were fasted for 4 h to remove the effects of food intake on glucose metabolism, and blood was taken from the tail vein at 18:00 h. In fasting experiments, mice were fasted for 24 h with free access to water. Then serum was immediately collected and stored at −20 °C. Blood glucose levels were measured by a glucose measurement device (Glucocard GT-1640, Arkray, Kyoto, Japan). The serum insulin concentrations were determined using kits from Morinaga (Tokyo, Japan).

Intraperitoneal Glucose Tolerance Test (ipGTT) and Insulin Tolerance Test (ITT)—For ipGTT, the mice were fasted for 16 h and received an intraperitoneal injection of D-glucose (1 g/kg body weight). The blood samples were collected from the tail vein before and at 15, 30, 60, and 120 min after the injection of D-glucose. For ITT, mice were fasted for 4 h and received an intraperitoneal injection of insulin (1 unit/kg body weight). The

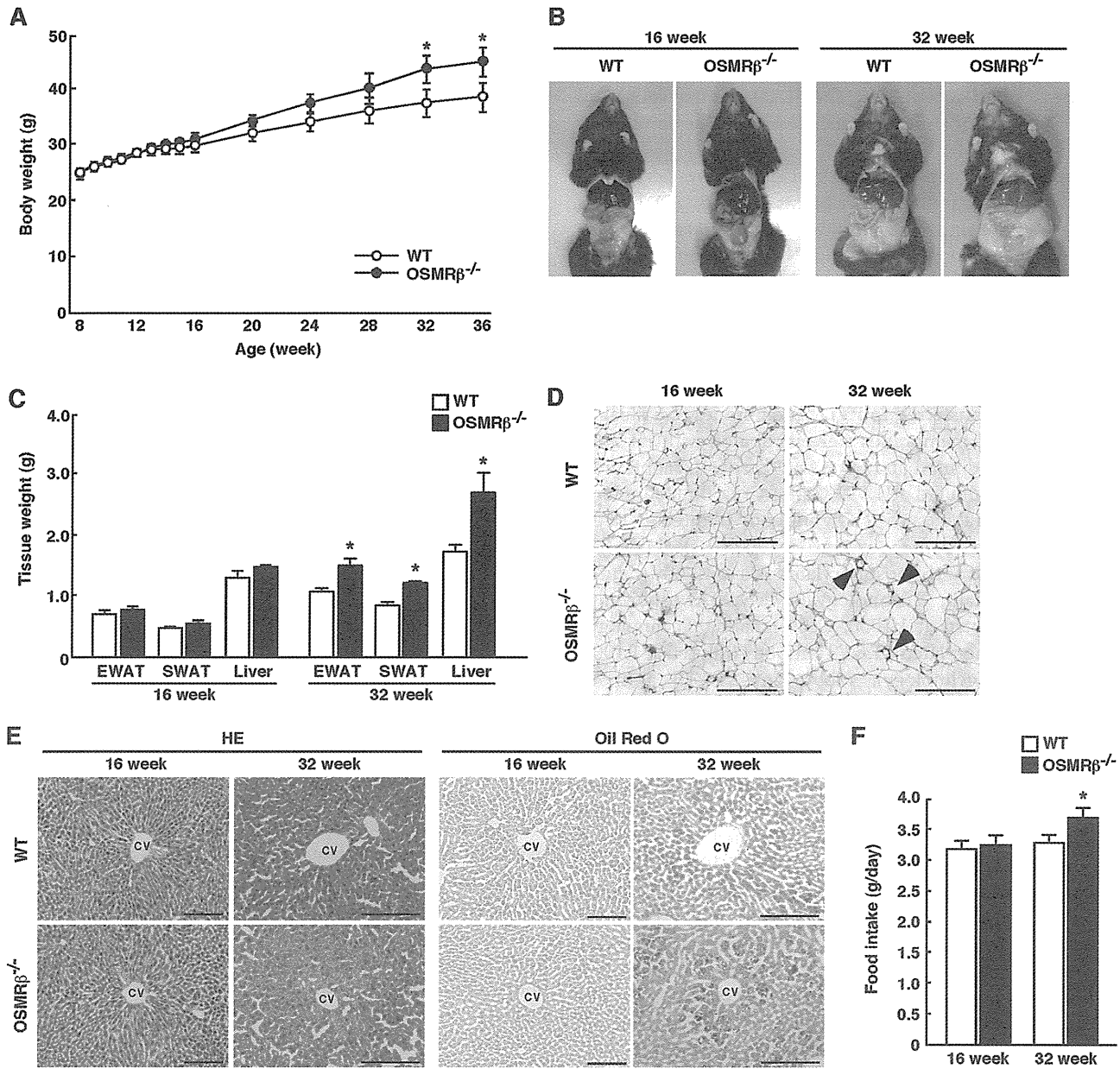

FIGURE 1. **The characteristics of WT and OSMR$\beta^{-/-}$ mice under normal diet conditions.** *A*, shown are the body weights of WT and OSMR$\beta^{-/-}$ mice from 8 to 36 weeks of age ($n = 6–10$). *B*, shown are representative images of WT and OSMR$\beta^{-/-}$ mice at 16 and 32 weeks of age. *C*, shown are the tissue weights in WT and OSMR$\beta^{-/-}$ mice at 16 and 32 weeks of age ($n = 6–10$). *EWAT*, epididymal white adipose tissue; *SWAT*, subcutaneous white adipose tissue. *D*, shown is a histological analysis with H&E (*HE*) staining in the EWAT in WT and OSMR$\beta^{-/-}$ mice at 16 and 32 weeks of age. *Arrowheads* indicate crown-like structures. *Scale bars* = 200 μm. *E*, shown is a histological analysis with H&E staining and Oil Red O staining in the liver of WT and OSMR$\beta^{-/-}$ mice at 16 and 32 weeks of age. *CV*, central vein. *Scale bars* = 100 μm. *F*, food intake in WT and OSMR$\beta^{-/-}$ mice at 16 and 32 weeks of age ($n = 6–10$) is shown. The data represent the mean ± S.E. *, $p < 0.05$ WT *versus* OSMR$\beta^{-/-}$ mice, ANOVA followed by the post-hoc Bonferroni test (A); Student's *t* test (*C* and *F*).

blood samples were collected from the tail vein before and at 15, 30, 60, and 120 min after the injection of insulin.

ELISA—Concentrations of serum TNF-α, IL-6, IL-10, adiponectin, and monocyte chemoattractant protein-1 (MCP-1) were measured by ELISA kits (R & D Systems) according to the manufacturer's instructions. The serum concentrations of leptin, serum amyloid A, and OSM were determined using ELISA kits from Morinaga, Invitrogen, and USCN Life Science (Wuhan, China), respectively.

Measurement of Lipid Content in the Serum and Liver—The serum levels of triglycerides, total cholesterol, and free fatty acids were measured at Nagahama Life Science Laboratory (Nagahama, Japan) using lipid assay kits (Triglyceride E-Test Wako, Total Cholesterol E-Test Wako, and NEFA C-Test Wako, Wako Pure Chemical Industries, Osaka, Japan) according to the manufacturer's instructions.

The contents of the triglycerides and total cholesterol in the liver were analyzed at Skylight Biotech (Akita, Japan). Lipids were extracted from the livers using the Folch method (29). Frozen liver tissues were homogenized, and triglycerides and total cholesterol were extracted from the homogenate with chloroform/methanol (2:1, v/v), dried, and resus-

TABLE 1

Various metabolic parameters in the serum and liver of WT and OSMR $\beta^{-/-}$ mice at 16 and 32 weeks of age ($n = 6-8$)

The data represent the mean ± S.E.

Parameters (units)	WT (16 weeks)	OSMR$\beta^{-/-}$ (16 weeks)	WT (32 weeks)	OSMR$\beta^{-/-}$ (32 weeks)
Serum concentrations				
Total cholesterol (mg/dl)	94.2 ± 8.1	90.2 ± 3.1	102.7 ± 4.6	141.3 ± 0.7[a]
Triglyceride (mg/dl)	107.0 ± 10.0	102.7 ± 13.1	87.7 ± 8.3	102.0 ± 5.8[a]
Free fatty acid (mmol/liter)	1.40 ± 0.16	1.51 ± 0.07	1.90 ± 0.02	1.98 ± 0.01[a]
Leptin (ng/ml)	5.97 ± 0.39	7.32 ± 1.63	12.6 ± 2.8	18.8 ± 2.5[a]
Serum amyloid A (ng/ml)	8.84 ± 1.74	14.24 ± 1.93[a]	14.9 ± 1.4	30.6 ± 6.4[a]
TNF-α (pg/ml)	3.61 ± 0.24	4.67 ± 0.45[a]	4.22 ± 0.62	5.69 ± 0.85[a]
IL-6 (pg/ml)	0.27 ± 0.05	0.31 ± 0.08	0.51 ± 0.06	0.68 ± 0.06[a]
MCP-1 (pg/ml)	20.1 ± 0.6	24.3 ± 2.1[a]	46.9 ± 7.6	84.2 ± 11.2[a]
IL-10 (pg/ml)	7.04 ± 0.57	5.55 ± 0.43[a]	10.6 ± 0.6	9.08 ± 0.61[a]
Adiponectin (μg/ml)	25.1 ± 2.1	22.2 ± 0.8[a]	15.3 ± 0.7	13.2 ± 0.5[a]
OSM (pg/ml)	64.7 ± 8.1	60.92 ± 7.7	46.9 ± 9.7	73.5 ± 11.8[a]
Glucose (fed) (mg/dl)	135.3 ± 12.7	152.0 ± 9.1	162.0 ± 16.3	198.3 ± 18.1[a]
Insulin (fed) (ng/ml)	0.66 ± 0.05	5.41 ± 1.60[a]	2.10 ± 0.11	9.98 ± 0.60[b]
Glucose (fasted) (mg/dl)	68.7 ± 2.6	64.0 ± 3.1	80.0 ± 4.2	89.7 ± 2.9[a]
Insulin (fasted) (ng/ml)	0.31 ± 0.09	2.21 ± 0.71[a]	0.96 ± 0.33	5.63 ± 0.21[b]
Liver concentrations				
Total cholesterol (mg/g)	2.03 ± 0.10	2.23 ± 0.06	2.10 ± 0.03	3.12 ± 0.20[a]
Triglyceride (mg/g)	9.82 ± 3.21	13.6 ± 2.9	15.2 ± 0.4	105.4 ± 18.4[b]

[a] $p < 0.05$ WT *versus* OSMR$\beta^{-/-}$ mice; Student's *t* test.
[b] $p < 0.01$ WT *versus* OSMR$\beta^{-/-}$ mice; Student's *t* test.

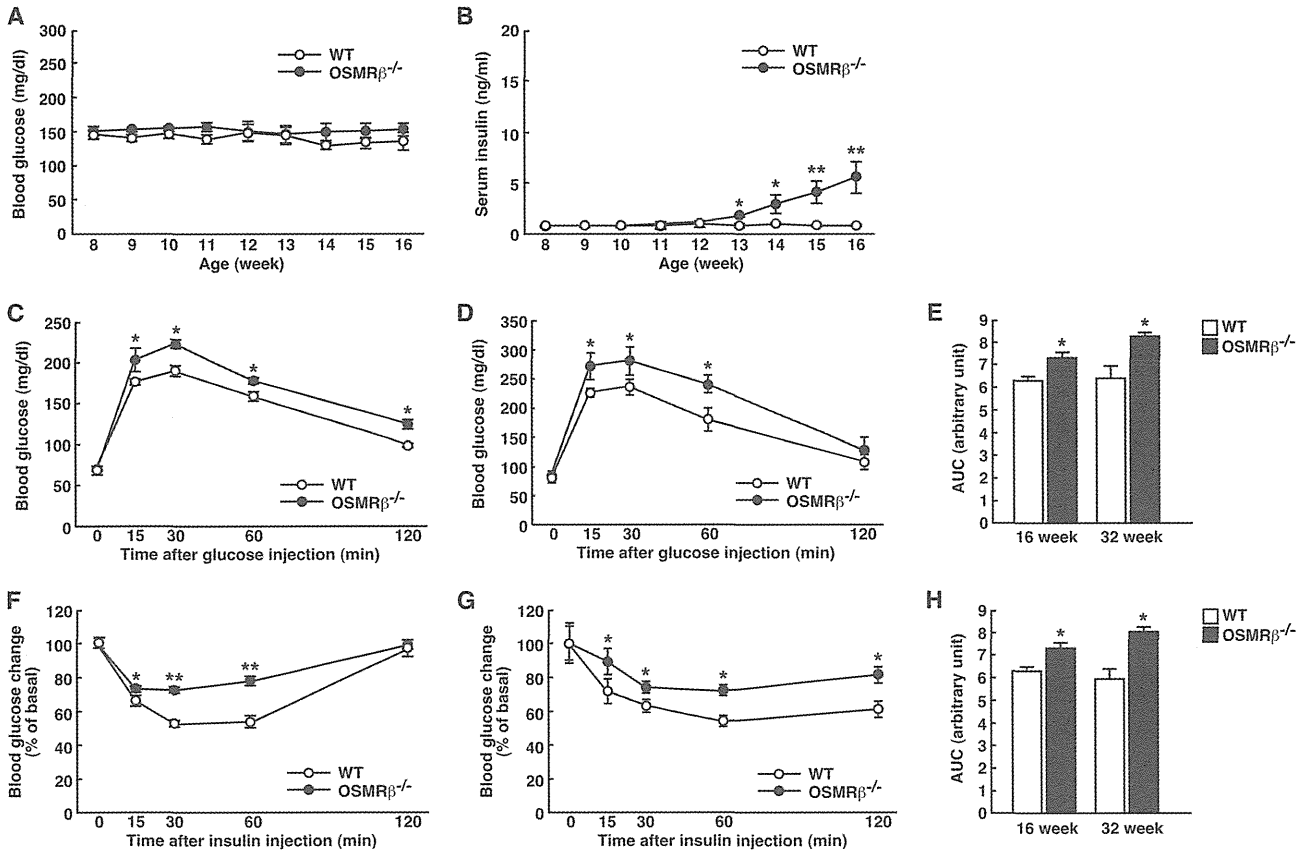

FIGURE 2. **Glucose intolerance and insulin resistance in OSMR$\beta^{-/-}$ mice under normal diet conditions.** *A* and *B*, shown are blood glucose (*A*) and serum insulin (*B*) levels in WT and OSMR$\beta^{-/-}$ mice from 8 to 16 weeks of age ($n = 6$). *C–H*, shown are the results of the ipGTTs (*C* and *D*) and ITTs (*F* and *G*) in WT and OSMR$\beta^{-/-}$ mice at 16 (*C* and *F*) and 32 (*D* and *G*) weeks of age ($n = 6$). The areas under the curves (*AUC*) for blood glucose in the ipGTTs (*E*) and ITTs (*H*) are shown. The data represent the mean ± S.E. *, $p < 0.05$; **, $p < 0.01$ WT *versus* OSMR$\beta^{-/-}$ mice, ANOVA followed by the post-hoc Bonferroni test (*A–D*, *F*, and *G*); Student's *t* test (*E* and *H*).

pended in 2-propanol. The amounts of triglycerides and total cholesterol in the extract were measured using lipid assay kits (Cholestest TG and Cholestest CHO, Sekisui Medical, Tokyo, Japan).

Quantitative Real-time PCR—Quantitative real-time PCR was performed with some modifications as described previously (25). Briefly, total RNAs from PEMs were prepared using TRI reagent (Molecular Research Center, Cincinnati,

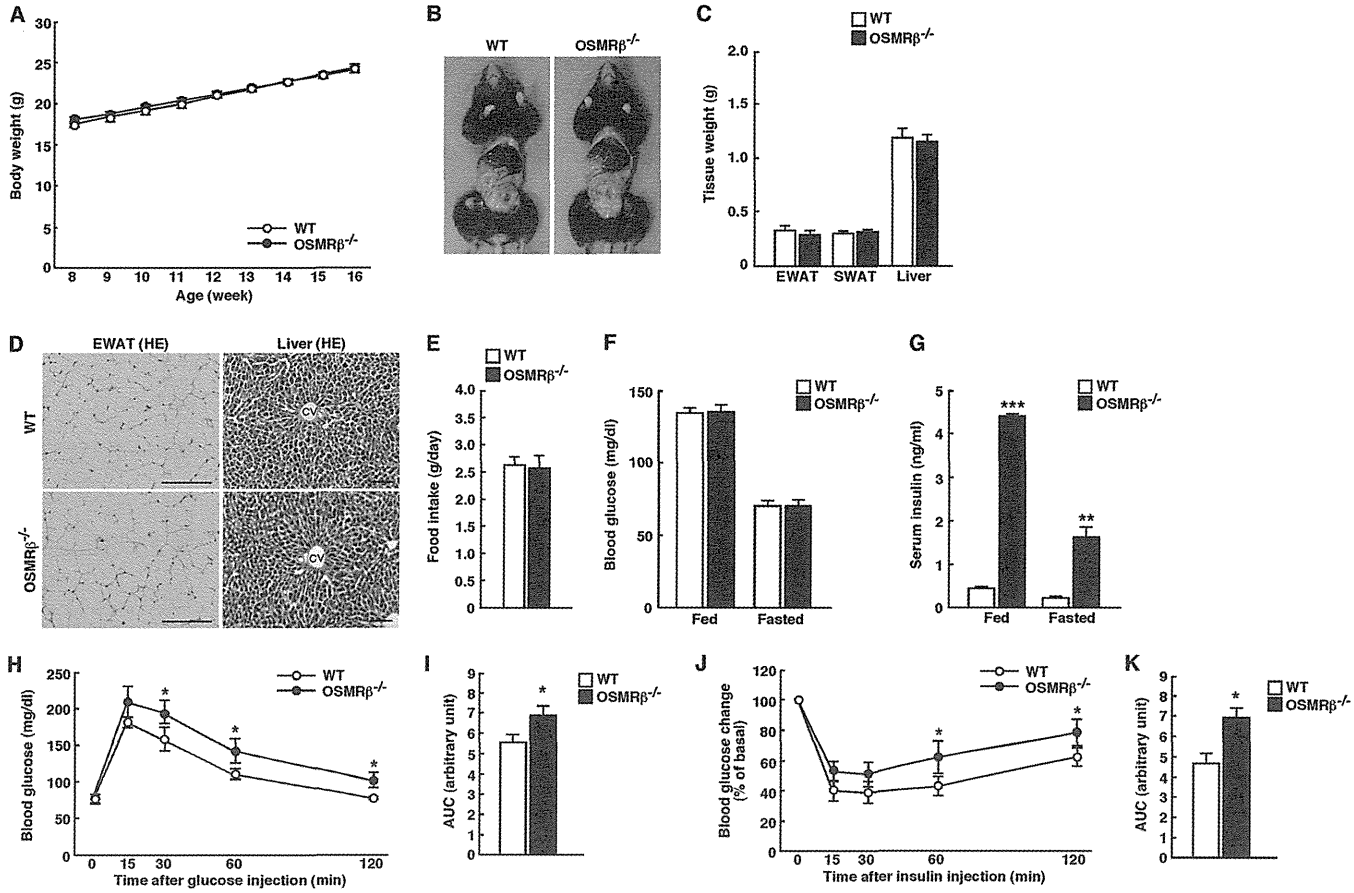

FIGURE 3. **The characteristics of female WT and OSMR$\beta^{-/-}$ mice under normal diet conditions.** *A*, shown are the body weights of female WT and OSMR$\beta^{-/-}$ mice from 8 to 16 weeks of age ($n = 6$). *B*, shown are representative images of female WT and OSMR$\beta^{-/-}$ mice at 16 weeks of age. *C*, shown are the tissue weights in female WT and OSMR$\beta^{-/-}$ mice at 16 weeks of age ($n = 6$). *EWAT*, epididymal white adipose tissue; *SWAT*, subcutaneous white adipose tissue. *D*, shown is a histological analysis with H&E (*HE*) staining in the epididymal white adipose tissue and liver in female WT and OSMR$\beta^{-/-}$ mice at 16 weeks of age. *CV*, central vein. *Scale bars* = 200 μm (epididymal white adipose tissue); 100 μm (liver). *E*, shown is food intake in female WT and OSMR$\beta^{-/-}$ mice at 16 weeks of age ($n = 6$). *F* and *G*, shown are blood glucose (*F*) and serum insulin (*G*) levels in female WT and OSMR$\beta^{-/-}$ mice at 16 weeks of age under fed and fasted conditions. *H–K*, shown are the results of the ipGTTs (*H*) and ITTs (*J*) in female WT and OSMR$\beta^{-/-}$ mice at 16 weeks of age ($n = 6$). The areas under the curves (*AUC*) for blood glucose in the ipGTTs (*I*) and ITTs (*K*) are shown. The data represent the mean ± S.E. *, $p < 0.05$; **, $p < 0.01$; ***, $p < 0.005$ WT *versus* OSMR$\beta^{-/-}$ mice, ANOVA followed by the post-hoc Bonferroni test (*A*, *H*, and *J*); Student's *t* test (*C*, *E*, *F*, *G*, *I*, and *K*).

OH). The cDNA from the total RNA was synthesized with TaqMan Reverse Transcription Reagents (Applied Biosystems, Foster City, CA). The following TaqMan Gene Expression Assays (Applied Biosystems) were used: TNF-α (Mm00443258_m1), IL-1β (Mm00434228_m1), IFN-γ (Mm00801778_m1), MCP-1 (Mm00441242_m1), C-C chemokine receptor 2 (CCR2) (Mm00438270_m1), toll-like receptor 4 (TLR4) (Mm00445273_m1), IL-6 (Mm00446190_m1), IL-10 (Mm00439616_m1), IL-13 (Mm00434204_m1), adiponectin (Mm00456425_m1), macrophage galactose-type C-type lectin (MGL) 1 (Mm00546124_m1), MGL2 (Mm00460844_m1), OSM (Mm01193966_m1), OSMRβ (Mm00495424_m1), and 18 S (Hs99999901_s1). Quantitative real-time PCR for each gene was performed using Rotor Gene Q (Qiagen, Hilden, Germany) and Rotor Gene Probe PCR kits (Qiagen). The PCR amplification protocol was 95 °C for 10 min and then 40 cycles of 95 °C for 10 s and 60 °C for 45 s. The relative abundance of transcripts was normalized by the expression of 18 S mRNA and analyzed using ΔΔCT method.

Statistical Analysis—The results are shown as the means ± S.E. Statistically significant differences between groups were analyzed by Student's *t* test or an analysis of variance (ANOVA) followed by the post-hoc Bonferroni test. The criterion for statistical significance was $p < 0.05$.

RESULTS

Systemic Changes of Metabolic Parameters in OSMR$\beta^{-/-}$ Mice—To assess the roles of OSMRβ in the metabolic diseases, we analyzed OSMR$\beta^{-/-}$ mice under normal diet conditions. The macroscopic findings, body weights, and tissue weights (epididymal adipose tissue, subcutaneous adipose tissue, and liver) did not differ significantly between WT and OSMR$\beta^{-/-}$ mice until 16 weeks of age (Fig. 1, *A–C*). However, OSMR$\beta^{-/-}$ mice began to be heavier than WT mice at 20 weeks of age, and the significant increase in body weights compared with WT mice was observed in OSMR$\beta^{-/-}$ mice at 32 weeks of age (Fig. 1*A*). At 32 weeks of age, the weights of the adipose tissue and liver in OSMR$\beta^{-/-}$ mice were heavier than those in WT mice (Fig. 1, *B* and *C*). As shown in Fig. 1*D*, in the adipose tissue of OSMR$\beta^{-/-}$ mice the adipocytes appeared to be larger than those in WT mice, and crown-like structures were also observed. In addition, lipid accumulation was greater in the

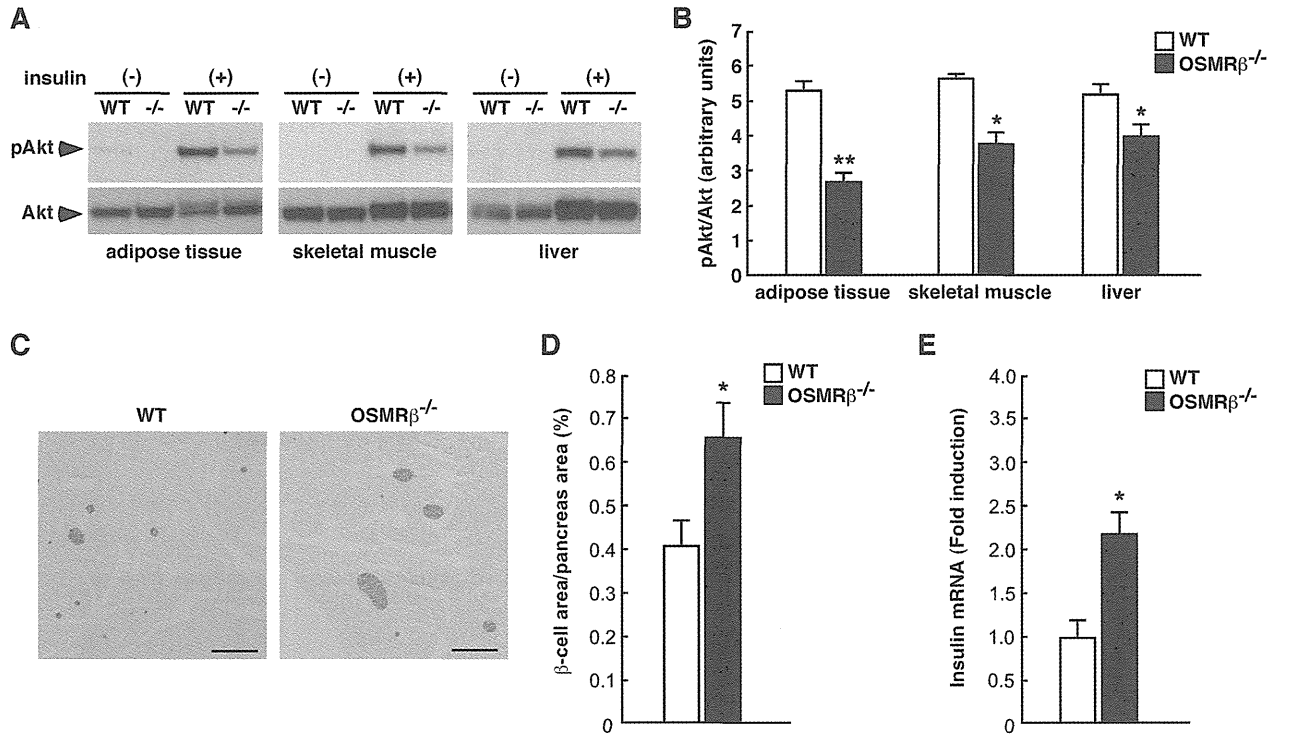

FIGURE 4. **Reduced insulin signaling and pancreatic β-cell hyperplasia in OSMRβ$^{-/-}$ mice at 16 weeks of age under normal diet conditions.** *A*, shown is insulin-stimulated Akt phosphorylation in the adipose tissue, skeletal muscle, and liver of WT and OSMRβ$^{-/-}$ mice. *B*, shown is quantitative analysis of phosphorylation of Akt in the adipose tissue, skeletal muscle, and liver of WT and OSMRβ$^{-/-}$ mice ($n = 6$). *C–E*, shown are hyperplasia of β-cells and insulin production in the pancreas of WT and OSMRβ$^{-/-}$ mice. *C*, shown is immunohistochemistry for insulin (*black*) in the pancreas of WT and OSMRβ$^{-/-}$ mice. Scale bars = 500 μm. *D*, shown is quantitative analysis of the area of β-cells in the total area of the pancreas. *E*, shown is the mRNA expression of insulin in the pancreas of WT and OSMRβ$^{-/-}$ mice. The data represent the mean ± S.E. *, $p < 0.05$; **, $p < 0.01$ WT *versus* OSMRβ$^{-/-}$ mice, Student's *t* test (*B*, *D*, and *E*).

livers of OSMRβ$^{-/-}$ mice compared with that in WT mice at 32 weeks of age (Fig. 1*E*). However, the adipose tissue and liver were histologically normal in OSMRβ$^{-/-}$ mice at 16 weeks of age (Fig. 1, *D* and *E*). Although there was no difference in the amount of food intake between WT and OSMRβ$^{-/-}$ mice at 16 weeks of age, OSMRβ$^{-/-}$ mice showed hyperphagia at 32 weeks of age (Fig. 1*F*).

The serum concentration of leptin in OSMRβ$^{-/-}$ mice was higher than that in WT mice at 32 weeks of age, although it was not changed between WT and OSMRβ$^{-/-}$ mice at 16 weeks of age (Table 1). Both serum lipid levels (total cholesterol, triglyceride, and free fatty acid) and lipid contents in the liver (total cholesterol and triglyceride) were higher in OSMRβ$^{-/-}$ mice at 32 weeks of age (Table 1). Neither the serum lipid levels nor lipid contents in the liver were different between WT and OSMRβ$^{-/-}$ mice at 16 weeks of age (Table 1).

To investigate the systemic inflammation in OSMRβ$^{-/-}$ mice, we analyzed the serum levels of some inflammatory markers. The serum concentrations of serum amyloid A, TNF-α, IL-6, and MCP-1 were higher, whereas the concentrations of IL-10 and adiponectin in the serum were lower in OSMRβ$^{-/-}$ mice than in WT mice at 32 weeks of age (Table 1). The changes in those inflammatory markers, except for IL-6, were already observed at 16 weeks of age (Table 1). Serum concentration of IL-6 also tended to increase but not significantly in OSMRβ$^{-/-}$ mice at 16 weeks of age (Table 1).

At 32 weeks of age, both blood glucose and serum insulin levels in fed and fasted conditions were higher in OSMRβ$^{-/-}$ mice compared with those in WT mice (Table 1). At 16 weeks of age, there were no differences in blood glucose levels between WT and OSMRβ$^{-/-}$ mice, whereas serum insulin levels were higher in OSMRβ$^{-/-}$ mice in both fed and fasted conditions (Table 1).

Similar to the male mice, neither female WT nor female OSMRβ$^{-/-}$ mice showed any differences in body weight, tissue weights, or food intake (see Fig. 3, *A–E*). The blood glucose levels did not differ between WT and OSMRβ$^{-/-}$ mice; however, the serum insulin levels were increased in OSMRβ$^{-/-}$ mice in fed and fasted conditions at 16 weeks of age (see Fig. 3, *F* and *G*). These results suggest that OSMRβ$^{-/-}$ mice exhibit systemic inflammation and disturbance of glucose metabolism preceding obesity. We next analyzed glucose and insulin levels in more detail.

OSMRβ$^{-/-}$ Mice Develop Glucose Intolerance and Insulin Resistance—To examine the effects of OSMRβ deficiency on glucose metabolism, we measured the blood glucose and serum insulin levels once a week for 8 weeks in WT and OSMRβ$^{-/-}$ mice under normal diet conditions. As shown in Fig. 2*A*, there were no significant changes in the blood glucose levels between WT and OSMRβ$^{-/-}$ mice until 16 weeks of age. However, the serum insulin levels began to increase in OSMRβ$^{-/-}$ mice compared with those observed in WT mice starting from 13 weeks of age (Fig. 2*B*). In addition, ipGTTs and ITTs revealed that OSMRβ$^{-/-}$ mice displayed glucose intolerance and insulin resistance at both 16 and 32 weeks of age (Fig. 2, *C–H*). Consistent with the data in the male mice, the female

OSMR$\beta^{-/-}$ mice at 16 weeks of age exhibited glucose intolerance and insulin resistance, as measured with ipGTTs and ITTs (Fig. 3, *H–K*).

To investigate the tissue-specific insulin resistance in OSMR$\beta^{-/-}$ mice at 16 weeks of age, we analyzed insulin-stimulated Akt phosphorylation in the adipose tissue, skeletal

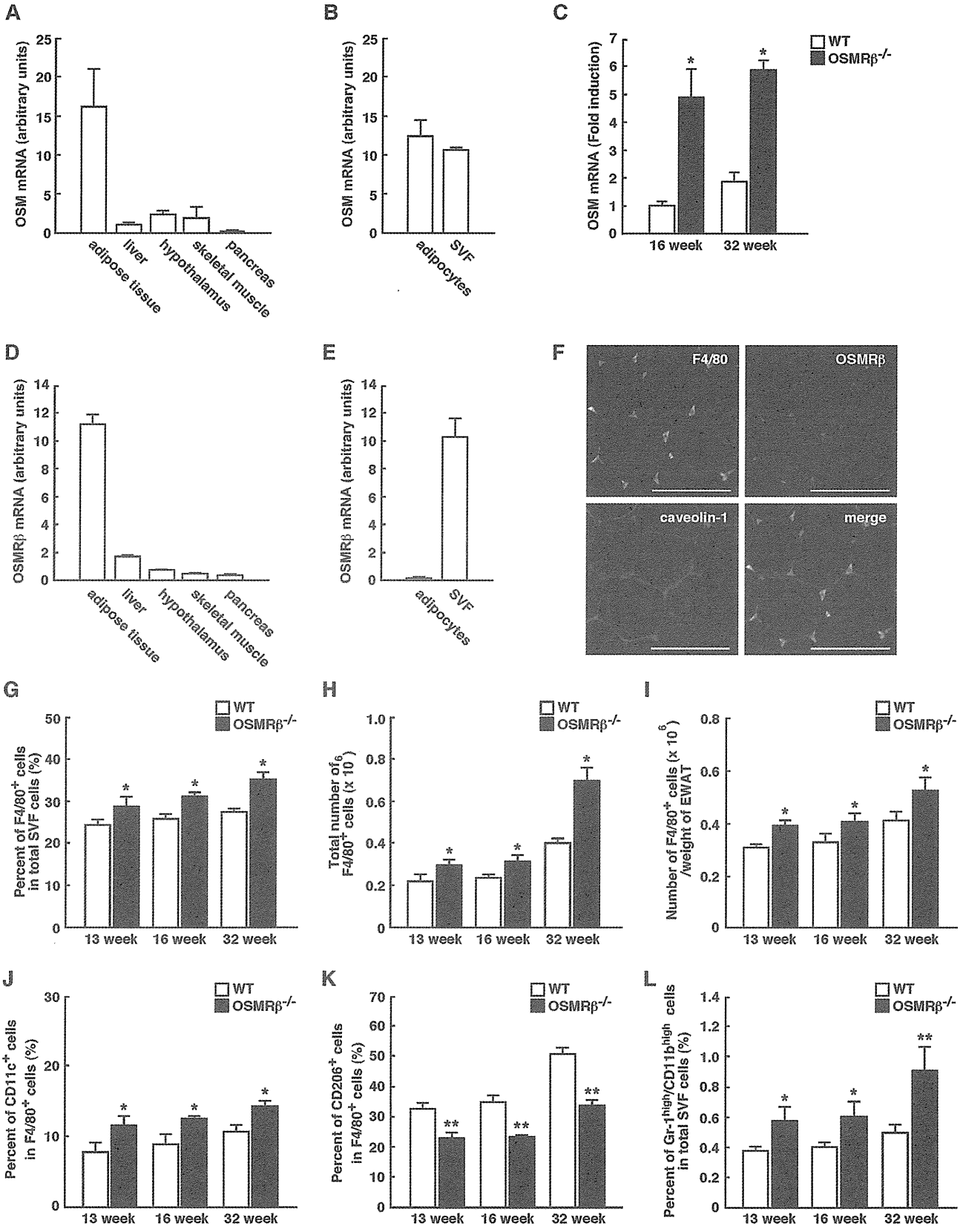

muscle, and liver. Insulin-stimulated Akt phosphorylation was decreased in the adipose tissue, skeletal muscle, and liver in OSMR$\beta^{-/-}$ mice compared with that observed in WT mice (Fig. 4, *A* and *B*). Histological examination of pancreas revealed that the percentages of insulin-positive areas (β-cells) among total areas of the pancreas were higher in OSMR$\beta^{-/-}$ mice compared with those in WT mice at 16 weeks of age (Fig. 4, *C* and *D*), suggesting that OSMR$\beta^{-/-}$ mice exhibit hyperplasia of β-cells in the pancreas. In addition, the expression of insulin mRNA was increased in the pancreas of OSMR$\beta^{-/-}$ mice compared with that in WT mice at 16 weeks of age (Fig. 4*E*).

Adipose Tissue Inflammation and Phenotypes of ATMs in OSMR$\beta^{-/-}$ Mice—It is well established that obesity-induced adipose tissue inflammation is important for the development of insulin resistance (5). Both OSM and OSMRβ were expressed strongly in the adipose tissue and little in the liver, hypothalamus, skeletal muscle, and pancreas at 16 weeks of age (Fig. 5, *A* and *D*). In the adipose tissue, the expression of OSM was observed in both SVF and adipocyte fractions (Fig. 5*B*). In contrast, OSMRβ was mainly expressed in the SVF, whereas the expression of OSMRβ was rarely detected in the adipocyte fraction (Fig. 5*E*).

Serum concentration of OSM was not changed between WT and OSMR$\beta^{-/-}$ mice at 16 weeks of age (Table 1). However, the expression of OSM mRNA in the adipose tissue was increased in OSMR$\beta^{-/-}$ mice compared with that in WT mice (Fig. 5*C*). At 32 weeks of age, both serum concentration of OSM and the expression of OSM mRNA in the adipose tissue were higher in OSMR$\beta^{-/-}$ mice compared with those in WT mice (Fig. 5*C* and Table 1).

In addition, double-immunofluorescence staining revealed that OSMRβ was exclusively expressed in F4/80-positive macrophages in the adipose tissue (Fig. 5*F*). Therefore, OSM appears to act primarily on macrophages in the adipose tissue.

Next we examined the phenotypes of ATMs in OSMR$\beta^{-/-}$ mice under normal diet conditions. The flow cytometric analyses of the SVF showed that the percentages and total numbers of F4/80-positive cells were increased in OSMR$\beta^{-/-}$ mice compared with those observed in WT mice at 13, 16, and 32 weeks of age (Fig. 5, *G–I*). To discriminate between M1 and M2 ATMs with flow cytometry, we used antibodies against CD11c and CD206 as markers of M1 and M2 ATMs, respectively (15). The percentages of CD11c-positive M1 ATMs among the total numbers of ATMs were higher in OSMR$\beta^{-/-}$ mice than in WT mice (Fig. 5*J*). In contrast, the percentages of CD206-positive M2 ATMs among the total numbers of ATMs were lower in OSMR$\beta^{-/-}$ mice than in WT mice (Fig. 5*K*). In addition, the percentages of neutrophils, which highly expressed both Gr-1 and CD11b, among total SVF cells were higher in OSMR$\beta^{-/-}$ mice than in WT mice (Fig. 5*L*). Such changes in the phenotypes of ATMs were also observed at 13 weeks of age when serum insulin levels just started to rise (Fig. 5, *J–L*). These results indicate that OSMR$\beta^{-/-}$ mice exhibit phenotypic changes in ATMs to M1 at 13, 16, and 32 weeks of age.

To evaluate the adipose tissue inflammation in OSMR$\beta^{-/-}$ mice at 16 weeks of age, we examined the expression levels of various pro- and anti-inflammatory markers. The gene expressions of proinflammatory markers, including TNF-α, IL-1β, IFN-γ, MCP-1, CCR2, and TLR4, were more abundant in the adipose tissue and SVF of OSMR$\beta^{-/-}$ mice than in the adipose tissue and SVF of WT mice (Fig. 6, *A* and *B*). In contrast, the gene expressions of anti-inflammatory markers, including IL-10, IL-13, MGL1, and MGL2, in the adipose tissue and SVF of OSMR$\beta^{-/-}$ mice were lower than those observed in the adipose tissue and SVF of WT mice (Fig. 6, *A* and *B*). The gene expression of adiponectin in the adipose tissue also decreased in OSMR$\beta^{-/-}$ mice (Fig. 6*A*). There were no differences in the IL-6 gene expression levels in the adipose tissue and SVF between WT and OSMR$\beta^{-/-}$ mice (Fig. 6, *A* and *B*). Although iNOS was expressed more abundantly in the adipose tissue of OSMR$\beta^{-/-}$ mice than in the adipose tissue of WT mice, the expression levels of CD206 and CD163 were lower in OSMR$\beta^{-/-}$ mice (Fig. 6, *C* and *D*). These results indicate that OSMR$\beta^{-/-}$ mice exhibit adipose tissue inflammation under normal diet conditions.

To address the question of whether insulin resistance in OSMR$\beta^{-/-}$ mice resulted from inflammation in the adipose tissue, we treated OSMR$\beta^{-/-}$ mice with an anti-inflammatory agent, sodium salicylate. Both glucose intolerance and insulin resistance in OSMR$\beta^{-/-}$ mice were improved when the mice were treated with sodium salicylate (Fig. 6, *E–H*). These data suggest that inflammatory status in the adipose tissue is responsible for systemic insulin resistance of OSMR$\beta^{-/-}$ mice.

OSM Polarizes Macrophages to the M2 Phenotype—To investigate the effects of OSM on macrophage polarization, the expressions of several macrophage markers were determined in PEMs obtained from WT and OSMR$\beta^{-/-}$ mice. The expression of OSMRβ was observed in F4/80-positive cells in PEMs obtained from WT mice using flow cytometry (Fig. 7*A*). In addition, OSM activated STAT3 and CREB in PEMs obtained from WT mice but not in PEMs obtained from OSMR$\beta^{-/-}$ mice (Fig. 7*B*). Strikingly, the expressions of IL-10, MGL1, and MGL2 were markedly increased by OSM in PEMs obtained from WT mice (Fig. 7, *C–E*). In addition, OSM significantly increased the expression levels of arginase-1 and CD206 in

FIGURE 5. **Phenotypes of ATMs in WT and OSMR$\beta^{-/-}$ mice under normal diet conditions.** *A–F*, shown is expression of OSM and OSMRβ in the adipose tissue. *A*, shown is the mRNA expression of OSM in various tissues of C57BL/6J mice ($n = 6$). *B*, shown is mRNA expression of OSM in the SVF and adipocyte fraction in the adipose tissue of C57BL/6J mice ($n = 6$). *C*, shown is mRNA expression of OSM in the adipose tissue of WT and OSMR$\beta^{-/-}$ mice at 16 and 32 weeks of age ($n = 6$). *D*, shown is mRNA expression of OSMRβ in various tissues of C57BL/6J mice ($n = 6$). *E*, shown is mRNA expression of OSMRβ in the SVF and adipocyte fraction in the adipose tissue of C57BL/6J mice ($n = 6$). *F*, shown is immunofluorescence staining for OSMRβ (*red*) with F4/80 (*green*) and caveolin-1 (*blue*) in the adipose tissue of C57BL/6J mice. *Scale bars* = 100 μm. *G–I*, shown are the percentages (*G*) and total numbers (*H*) of F4/80-positive cells among the total numbers of cells in the SVF of the epididymal fat pads in WT and OSMR$\beta^{-/-}$ mice at 13, 16, and 32 weeks of age ($n = 4–6$). The total numbers of macrophages were normalized by the weights of the epididymal fat pads (*I*). *J* and *K*, shown are the percentages of CD11c-positive (*J*) and CD206-positive (*K*) cells in the F4/80-positive cells of WT and OSMR$\beta^{-/-}$ mice at 13, 16, and 32 weeks of age ($n = 4–6$). *L*, shown are the percentages of neutrophils (Gr-1^{high}/CD11b^{high} cells) in the total cells in the SVF of WT and OSMR$\beta^{-/-}$ mice at 13, 16, and 32 weeks of age ($n = 4–6$). The data represent the mean ± S.E. *, $p < 0.05$; **, $p < 0.01$ WT *versus* OSMR$\beta^{-/-}$ mice, Student's *t* test.

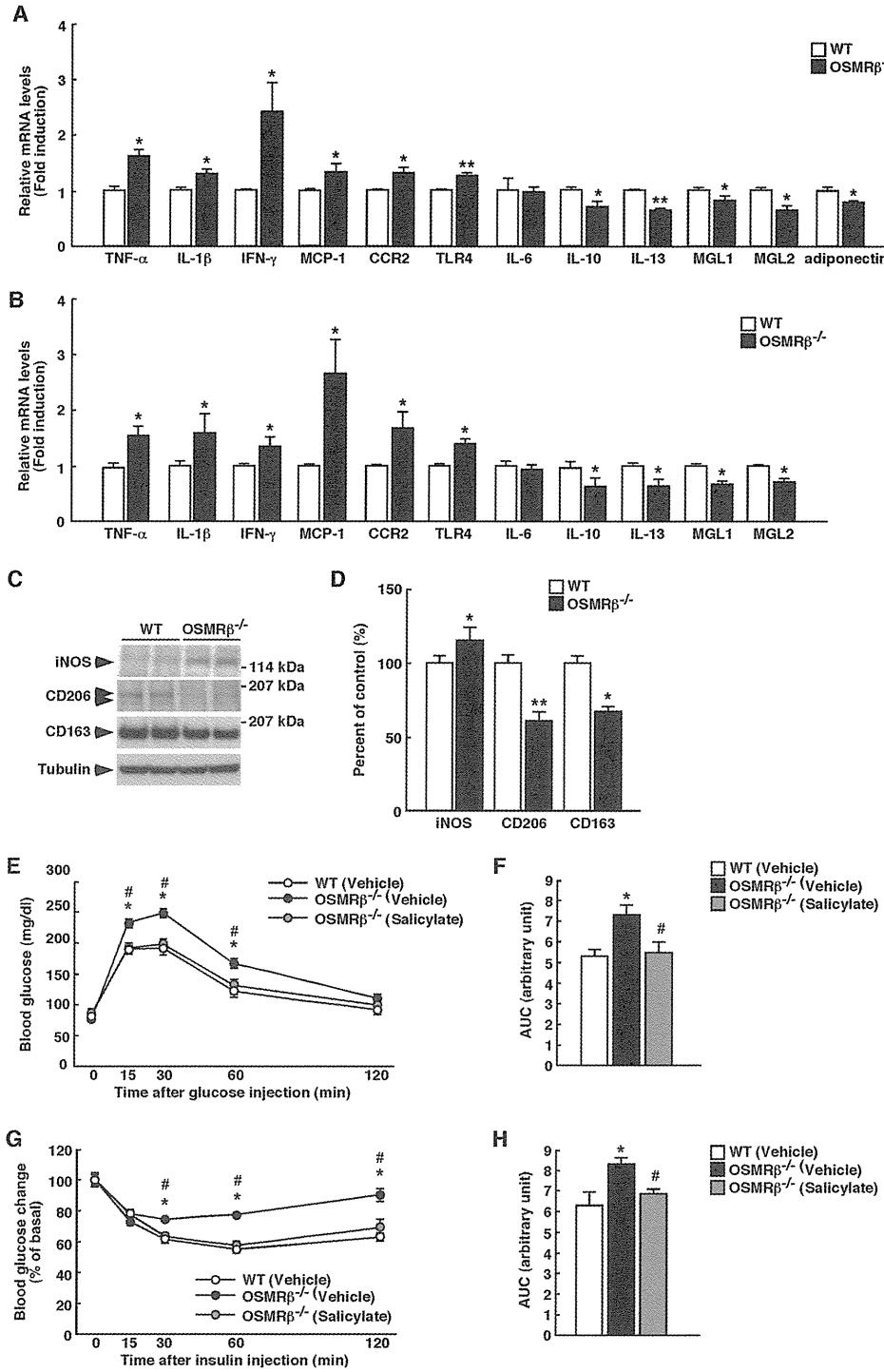

FIGURE 6. **Contribution of inflammatory status on insulin resistance in OSMR$\beta^{-/-}$ mice at 16 weeks of age.** *A* and *B*, shown are the expressions of proinflammatory markers (TNF-α, IL-1β, IFN-γ, MCP-1, CCR2, TLR4, and IL-6) and anti-inflammatory markers (IL-10, IL-13, MGL1, MGL2, and adiponectin) in the adipose tissue (*A*) and SVF (*B*) of WT and OSMR$\beta^{-/-}$ mice ($n = 6$). *C*, shown is Western blot analysis of markers of macrophage phenotypes (iNOS, CD206, and CD163) in the adipose tissue of WT and OSMR$\beta^{-/-}$ mice. The apparent molecular masses are indicated on the *right*. *D*, shown is quantitative analysis of the protein expression of iNOS, CD206, and CD163 ($n = 6$). *E–H*, shown are the effects of sodium salicylate on glucose intolerance and insulin resistance of OSMR$\beta^{-/-}$ mice. OSMR$\beta^{-/-}$ mice were injected intraperitoneally with either vehicle or sodium salicylate (120 μg/g body weight) once a day for 2 weeks. *E–H*, shown are the results of the ipGTTs (*E*) and ITTs (*G*) in OSMR$\beta^{-/-}$ mice injected with sodium salicylate. The areas under the curves (*AUC*) for blood glucose in the ipGTTs (*F*) and ITTs (*H*) are shown. The data represent the mean ± S.E. *, $p < 0.05$; **, $p < 0.01$ WT *versus* OSMR$\beta^{-/-}$ mice; #, $p < 0.05$ OSMR$\beta^{-/-}$ (*Vehicle*) *versus* OSMR$\beta^{-/-}$ (*Salicylate*) mice, ANOVA followed by the post-hoc Bonferroni test (*E* and *G*); Student's *t* test (*A*, *B*, *D*, *F*, and *H*).

PEMs obtained from WT mice (Fig. 7, *F* and *G*). The effects of OSM on the expressions of IL-10, MGL1, MGL2, arginase-1, and CD206 were completely abolished in PEMs obtained from OSMR$\beta^{-/-}$ mice (Fig. 7, *C–G*). The expression of iNOS, a marker of M1 macrophages, was not observed in PEMs regardless of whether the PEMs were

treated with OSM (Fig. 7*F*). In addition to that observed in PEMs, OSM induced the expressions of arginase-1 and CD206 in RAW264.7 cells, a mouse macrophage cell line (Fig. 7, *H* and *I*). OSM also increased the expressions of arginase-1 and CD206 and decreased the expression of iNOS in LPS-stimulated RAW264.7 cells (Fig. 7, *H* and *I*). Therefore, OSM can polarize the phenotypes of macrophages to M2.

OSM Polarizes ATMs to M2 Phenotype and Increases Insulin Sensitivity in Vivo—To investigate the effects of OSM on insulin sensitivity and phenotypic changes of ATMs, we treated

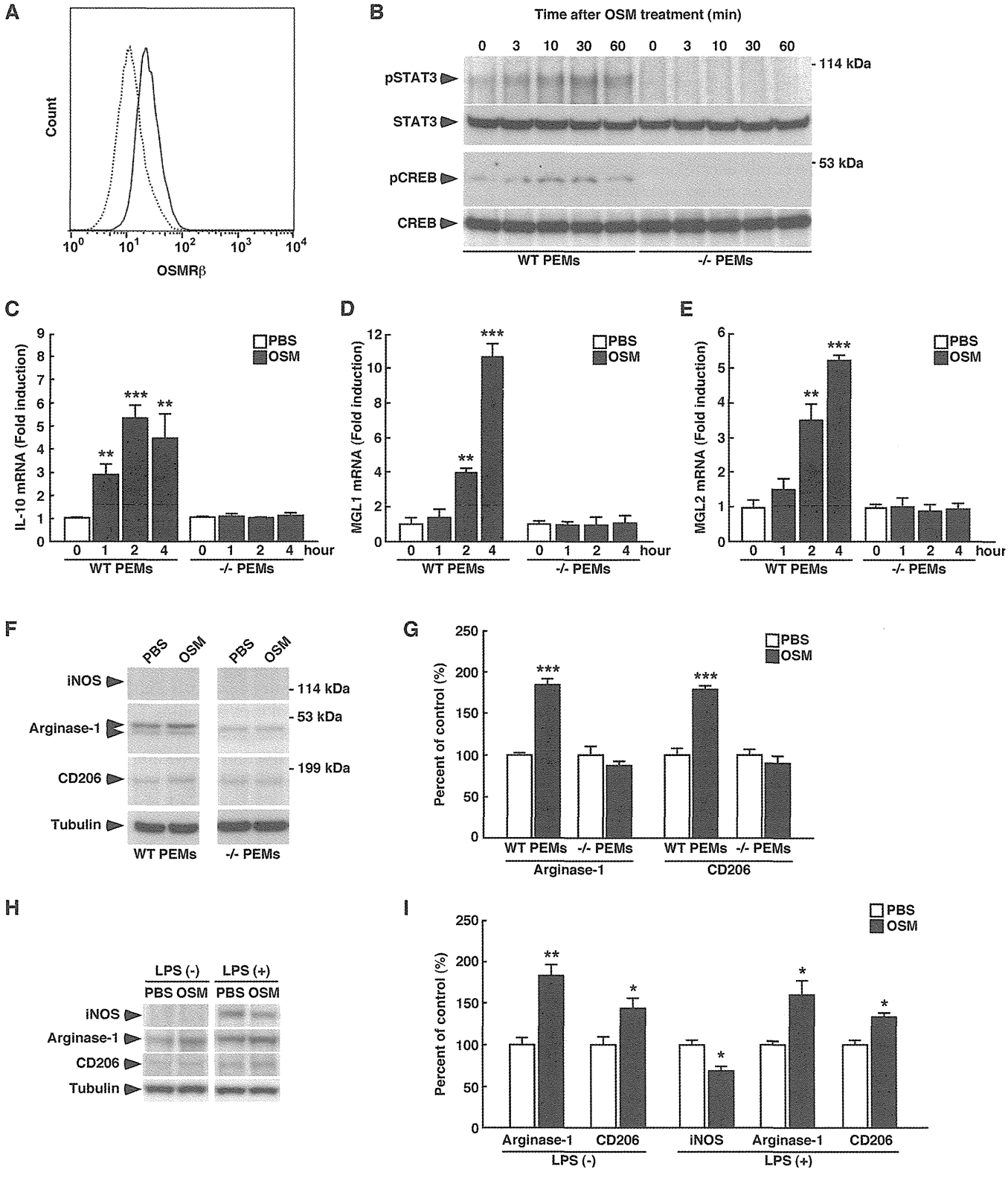

C57BL/6J mice with OSM for 1 week. Both glucose tolerance and insulin sensitivity in C57BL/6J mice were increased when the mice were treated with OSM (Fig. 8, *A–D*). In addition, both percentages and total numbers of F4/80-positive cells were reduced in mice treated with OSM (Fig. 8, *E–G*). The treatment with OSM increased the percentage of M2 ATMs but decreased the percentage of M1 ATMs in the adipose tissue (Fig. 8, *H* and *I*). In addition, OSM increased the expression of IL-10, IL-13, MGL1, and MGL2 in the adipose tissue (Fig. 8*J*). These data suggest that OSM can change the phenotypes of ATMs to M2 and increase insulin sensitivity *in vivo*.

DISCUSSION

OSM belongs to the IL-6 family of cytokines, including IL-6, IL-11, leukemia inhibitory factor, ciliary neurotrophic factor, and cardiotrophin-1 (30) and exhibits a variety of physiological functions, including the development of neurons and hepatocytes, hematopoiesis, and the modulation of inflammatory responses (21, 31–33). Although some members in this family, IL-6, ciliary neurotrophic factor, and cardiotrophin-1, are known to be associated with the development of obesity and insulin resistance (34–36), the role of OSM in these metabolic disturbances remains unclear. In this paper we have addressed this question using OSMR$\beta^{-/-}$ mice. OSMR$\beta^{-/-}$ mice exhibited obesity and insulin resistance at 32 weeks of age. Interestingly, insulin resistance preceding obesity was already observed in OSMR$\beta^{-/-}$ mice at 16 weeks of age.

It is well established that the balance between pro- and anti-inflammatory cytokines secreted from the adipose tissue is important for systemic insulin sensitivity. Proinflammatory cytokines, including TNF-α, IL-1β, and IFN-γ, promote the development of insulin resistance (16, 17, 37–40), whereas an anti-inflammatory cytokine, IL-10, improves obesity-induced insulin resistance (18). In the adipose tissue, these pro- and anti-inflammatory cytokines are produced by M1 and M2 macrophages, respectively (15). In the present study we found that the percentage of M1 macrophages and the expression of proinflammatory cytokines were increased in the adipose tissue of OSMR$\beta^{-/-}$ mice compared with WT mice. In contrast, the percentage of M2 macrophages and the expression of IL-10 were reduced in the adipose tissue of OSMR$\beta^{-/-}$ mice. Treatment of OSMR$\beta^{-/-}$ mice with sodium salicylate improved their insulin resistance, suggesting that systemic inflammation is important for the development of insulin resistance in OSMR$\beta^{-/-}$ mice. In addition, OSM was shown to directly polarize the phenotype of PEMs and RAW264.7 cells to M2. Furthermore, insulin sensitivity and the percentage of M2 ATMs were increased by the treatment with OSM *in vivo*. These findings suggest that OSM plays an important role in the regulation of energy homeostasis by insulin at least in part through the regulation of M1/M2 balance. In addition, Gr-1^{high}/CD11b^{high} cells, which are considered to be activated neutrophils, increased in the adipose tissue of OSMR$\beta^{-/-}$ mice. The increase of Gr-1^{high}/CD11b^{high} cells may contribute to drive or sustain the adipose tissue inflammation in OSMR$\beta^{-/-}$ mice.

As OSM is known to inhibit the differentiation of preadipocytes to mature adipocytes *in vitro* (41), our initial hypothesis was that OSM might reduce adiposity. However, there were no differences in the weight of adipose tissue between WT and OSMR$\beta^{-/-}$ mice under normal diet conditions. Most of the OSMRβ-positive cells were F4/80-positive macrophages, and few Dlk-1-positive preadipocytes were found in the adipose tissue. Furthermore, the phenotypes of the ATMs were polarized from M2 to M1 in OSMR$\beta^{-/-}$ mice fed a normal diet. These results suggest that macrophages play a more important role in the regulation of energy metabolism by OSM than do preadipocytes under normal diet conditions.

IL-6 potentially acts as a proinflammatory cytokine and induces hepatic insulin resistance in rodents (42, 43). However, chronic treatment of mice with IL-6 does not affect the insulin signaling in the skeletal muscle (42). In addition, IL-6-deficient mice showed systemic insulin resistance (34, 44). Therefore, the role of IL-6 in the development of systemic insulin resistance is controversial. In the present study, the IL-6 levels did not change in the adipose tissue of OSMR$\beta^{-/-}$ mice compared with those observed in the controls at 16 weeks of age when systemic insulin resistance developed in OSMR$\beta^{-/-}$ mice. By contrast, some proinflammatory cytokines (TNF-α, IL-1β, and IFN-γ), known to contribute to the development of insulin resistance (16, 17, 37–40), was significantly increased in the adipose tissue of OSMR$\beta^{-/-}$ mice. Therefore, IL-6 may function in the development of adipose tissue inflammation and insulin resistance in a manner distinct from that exhibited by other proinflammatory cytokines, including TNF-α, IL-1β, and IFN-γ. These observations suggest that our mouse model of metabolic syndrome with different expression patterns of proinflammatory cytokines may help in understanding functional differences between IL-6 and other proinflammatory cytokines in adipose tissue inflammation and insulin resistance.

The food intake is regulated by the hypothalamus and other associated regions of the brain, including the mesolimbic region and the brain stem (45). It has been reported that OSMRβ is expressed in a hypothalamic neuronal cell line, Gnv-4 cells (46). This finding raises the possibility that OSM

FIGURE 7. **The functional roles of OSM in macrophage.** *A*, shown is the expression of OSMRβ in PEMs obtained from WT mice. PEMs obtained from WT mice were stained with OSMRβ (*solid line*) or its control (*dotted line*) and analyzed by flow cytometry. *B*, shown is the activation of STAT3 and CREB by OSM in PEMs obtained from WT and OSMR$\beta^{-/-}$ mice. Western blot analysis of pSTAT3 and pCREB was performed in OSM-treated PEMs. The apparent molecular masses are indicated on the *right*. *C–E*, shown is the induction of IL-10 (*C*), MGL1 (*D*), and MGL2 (*E*) expression by OSM in PEMs. Quantitative real-time PCR was performed using mRNA prepared from OSM-treated PEMs obtained from WT and OSMR$\beta^{-/-}$ mice. *F*, shown are Western blot analyses of markers of macrophage phenotypes (iNOS, arginase-1, and CD206) in the OSM-treated PEMs obtained from WT and OSMR$\beta^{-/-}$ mice. The apparent molecular masses are indicated on the *right*. *G*, shown is quantitative analysis of the protein expression of arginase-1 and CD206. *H* and *I*, shown are the roles of OSM in RAW264.7 macrophages. *H*, shown is a Western blot analysis of markers of macrophage phenotypes (iNOS, arginase-1, and CD206) in non-stimulated or LPS-stimulated RAW264.7 macrophages. *I*, shown is a quantitative analysis of the protein expressions of iNOS, arginase-1, and CD206. The data represent the mean ± S.E. of three independent experiments. The data are expressed as percentages of control values (*white bars*). *, $p < 0.05$; **, $p < 0.01$; ***, $p < 0.005$ *versus* control, ANOVA followed by the post-hoc Bonferroni test (*C–E*); Student's *t* test (*G* and *I*).

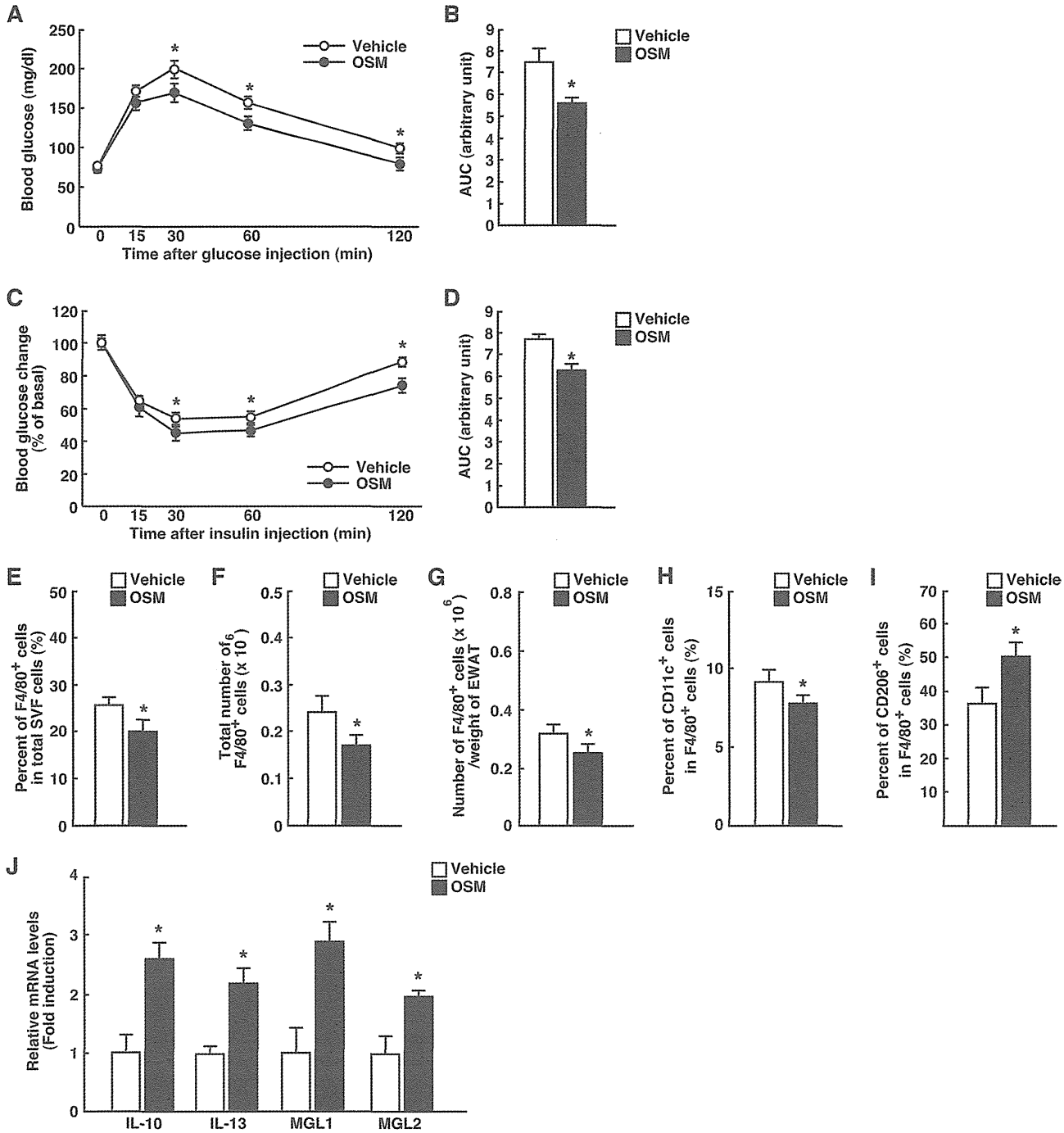

FIGURE 8. **Effects of OSM on phenotypes of ATMs and insulin sensitivity.** C57BL/6J mice were injected intraperitoneally with either vehicle or recombinant mouse OSM (12.5 ng/g body weight) twice a day for 1 week. *A–D*, shown are the results of the ipGTTs (*A*) and ITTs (*C*) in C57BL/6J mice injected with OSM ($n = 4$). The areas under the curves (*AUC*) for blood glucose in the ipGTTs (*B*) and ITTs (*D*) are shown. *E–G*, shown are the percentages (*E*) and total numbers (*F*) of F4/80-positive cells among the total numbers of cells in the SVF of the epididymal fat pads in C57BL/6J mice injected with OSM ($n = 4$). The total numbers of macrophages were normalized by the weights of the epididymal fat pads (*G*). *H* and *I*, shown are the percentages of CD11c-positive (*H*) and CD206-positive (*I*) cells in the F4/80-positive cells of C57BL/6J mice injected with OSM ($n = 4$). *J*, shown are the expressions of anti-inflammatory markers (IL-10, IL-13, MGL1, and MGL2) in the adipose tissue of C57BL/6J mice injected with OSM ($n = 4$). The data represent the mean ± S.E. *, $p < 0.05$ vehicle *versus* OSM, ANOVA followed by the post-hoc Bonferroni test (*A* and *C*); Student's *t* test (*B*, *D*, and *E–J*).

regulates food intake through the hypothalamus. However, we reported previously that OSMRβ is expressed only in the astrocytes of the olfactory bulb, the epithelial cells of the choroid plexus, and meningeal cells and not in the brain regions associated with food intake in normal adult mice (47). In addition, there were no significant differences in the food intake between WT and OSMR$\beta^{-/-}$ mice fed a normal diet at 16 weeks of age, suggesting that OSM signaling is unlikely to regulate food intake under the normal conditions.

It has been most widely accepted that obesity is a major risk factor for the development of insulin resistance (1), which is followed by hyperinsulinemia, the exhaustion of pancreatic β

cells, and then the development of type 2 diabetes. However, there are also some reports inconsistent with this obesity-induced model of the pathogenesis of type 2 diabetes in human; that is, insulin resistance without obesity or hyperinsulinemia preceding obesity (48, 49). Thus, the relationship between obesity, insulin resistance, and type 2 diabetes remains unclear yet. In addition, there are few reports in the mouse model that insulin resistance occurs preceding obesity. Although insulin resistance without obesity is observed in the mice deficient in insulin or insulin signaling genes, including Akt2, these mice do not exhibit systemic inflammation (50, 51). As systemic inflammation, hyperinsulinemia, and insulin resistance preceded obesity in OSMR$\beta^{-/-}$ mice, OSMR$\beta^{-/-}$ mice constitute a unique mouse model of metabolic diseases and may help to clarify a novel relationship among systemic inflammation, hyperinsulinemia, insulin resistance, and obesity.

REFERENCES

1. Després, J. P., and Lemieux, I. (2006) Abdominal obesity and metabolic syndrome. *Nature* **444,** 881–887
2. Elgazar-Carmon, V., Rudich, A., Hadad, N., and Levy, R. (2008) Neutrophils transiently infiltrate intra-abdominal fat early in the course of high-fat feeding. *J. Lipid Res.* **49,** 1894–1903
3. Talukdar, S., Oh da, Y., Bandyopadhyay, G., Li, D., Xu, J., McNelis, J., Lu, M., Li, P., Yan, Q., Zhu, Y., Ofrecio, J., Lin, M., Brenner, M. B., and Olefsky, J. M. (2012) Neutrophils mediate insulin resistance in mice fed a high-fat diet through secreted elastase. *Nat. Med.* **18,** 1407–1412
4. Lumeng, C. N., Maillard, I., and Saltiel, A. R. (2009) T-ing up inflammation in fat. *Nat. Med.* **15,** 846–847
5. Weisberg, S. P., McCann, D., Desai, M., Rosenbaum, M., Leibel, R. L., and Ferrante, A. W. Jr. (2003) Obesity is associated with macrophage accumulation in adipose tissue. *J. Clin. Invest.* **112,** 1796–1808
6. Hirasaka, K., Kohno, S., Goto, J., Furochi, H., Mawatari, K., Harada, N., Hosaka, T., Nakaya, Y., Ishidoh, K., Obata, T., Ebina, Y., Gu, H., Takeda, S., Kishi, K., and Nikawa, T. (2007) Deficiency of Cbl-b gene enhances infiltration and activation of macrophages in adipose tissue and causes peripheral insulin resistance in mice. *Diabetes* **56,** 2511–2522
7. Kanda, H., Tateya, S., Tamori, Y., Kotani, K., Hiasa, K., Kitazawa, R., Kitazawa, S., Miyachi, H., Maeda, S., Egashira, K., and Kasuga, M. (2006) MCP-1 contributes to macrophage infiltration into adipose tissue, insulin resistance, and hepatic steatosis in obesity. *J. Clin. Invest.* **116,** 1494–1505
8. Lesniewski, L. A., Hosch, S. E., Neels, J. G., de Luca, C., Pashmforoush, M., Lumeng, C. N., Chiang, S. H., Scadeng, M., Saltiel, A. R., and Olefsky J. M. (2007) Bone marrow-specific Cap gene deletion protects against high-fat diet-induced insulin resistance. *Nat. Med.* **13,** 455–462
9. Weisberg, S. P., Hunter, D., Huber, R., Lemieux, J., Slaymaker, S., Vaddi, K., Charo, I., Leibel, R. L., and Ferrante, A. W. Jr. (2006) CCR2 modulates inflammatory and metabolic effects of high-fat feeding. *J. Clin. Invest.* **116,** 115–124
10. Hamilton, T. A. (2002) in *The Macrophage* (Bourke, B., and Lewis, C. eds) pp. 73–102, Oxford University Press, Oxford
11. Gordon, S. (2003) Alternative activation of macrophages. *Nat. Rev. Immunol.* **3,** 23–35
12. Modolell, M., Corraliza, I. M., Link, F., Soler, G., and Eichmann, K. (1995) Reciprocal regulation of the nitric oxide synthase/arginase balance in mouse bone marrow-derived macrophages by TH1 and TH2 cytokines. *Eur. J. Immunol.* **25,** 1101–1104
13. Munder, M., Eichmann, K., and Modolell, M. (1998) Alternative metabolic states in murine macrophages reflected by the nitric oxide synthase/arginase balance. Competitive regulation by CD4+ T cells correlates with Th1/Th2 phenotype. *J. Immunol.* **160,** 5347–5354
14. Lumeng, C. N., Bodzin, J. L., and Saltiel, A. R. (2007) Obesity induces a phenotypic switch in adipose tissue macrophage polarization. *J. Clin. Invest.* **117,** 175–184
15. Fujisaka, S., Usui, I., Bukhari, A., Ikutani, M., Oya, T., Kanatani, Y., Tsuneyama, K., Nagai, Y., Takatsu, K., Urakaze, M., Kobayashi, M., and Tobe, K. (2009) Regulatory mechanisms for adipose tissue M1 and M2 macrophages in diet-induced obese mice. *Diabetes* **58,** 2574–2582
16. de Alvaro, C., Teruel, T., Hernandez, R., and Lorenzo, M. (2004) Tumor necrosis factor-α produces insulin resistance in skeletal muscle by activation of inhibitor κB kinase in a p38 MAPK-dependent manner. *J. Biol. Chem.* **279,** 17070–17078
17. Nguyen, M. T., Satoh, H., Favelyukis, S., Babendure, J. L., Imamura, T., Sbodio, J. I., Zalevsky, J., Dahiyat, B. I., Chi, N. W., and Olefsky, J. M. (2005) JNK and tumor necrosis factor-α mediate free fatty acid-induced insulin resistance in 3T3-L1 adipocytes. *J. Biol. Chem.* **280,** 35361–35371
18. Hong, E. G., Ko, H. J., Cho, Y. R., Kim, H. J., Ma, Z., Yu, T. Y., Friedline, R. H., Kurt-Jones, E., Finberg, R., Fischer, M. A., Granger, E. L., Norbury, C. C., Hauschka, S. D., Philbrick, W. M., Lee, C. G., Elias, J. A., and Kim, J. K. (2009) Interleukin-10 prevents diet-induced insulin resistance by attenuating macrophage and cytokine response in skeletal muscle. *Diabetes* **58,** 2525–2535
19. Tanaka, M., Hara, T., Copeland, N. G., Gilbert, D. J., Jenkins, N. A., and Miyajima, A. (1999) Reconstitution of the functional mouse oncostatin M (OSM) receptor. Molecular cloning of the mouse OSM receptor β subunit. *Blood* **93,** 804–815
20. Tamura, S., Morikawa, Y., Miyajima, A., and Senba, E. (2002) Expression of oncostatin M in hematopoietic organs. *Dev. Dyn.* **225,** 327–331
21. Wallace, P. M., MacMaster, J. F., Rouleau, K. A., Brown, T. J., Loy, J. K., Donaldson, K. L., and Wahl, A. F. (1999) Regulation of inflammatory responses by oncostatin M. *J. Immunol.* **162,** 5547–5555
22. Dillon, S. R., Sprecher, C., Hammond, A., Bilsborough, J., Rosenfeld-Franklin, M., Presnell, S. R., Haugen, H. S., Maurer, M., Harder, B., Johnston, J., Bort, S., Mudri, S., Kuijper, J. L., Bukowski, T., Shea, P., Dong, D. L., Dasovich, M., Grant, F. J., Lockwood, L., Levin, S. D., LeCiel, C., Waggie, K., Day, H., Topouzis, S., Kramer, J., Kuestner, R., Chen, Z., Foster, D., Parrish-Novak, J., and Gross, J. A. (2004) Interleukin 31, a cytokine produced by activated T cells, induces dermatitis in mice. *Nat. Immunol.* **5,** 752–760
23. Tanaka, M., Hirabayashi, Y., Sekiguchi, T., Inoue, T., Katsuki, M., and Miyajima, A. (2003) Targeted disruption of oncostatin M receptor results in altered hematopoiesis. *Blood* **102,** 3154–3162
24. Morikawa, Y., Furotani, M., Matsuura, N., and Kakudo, K. (1993) The role of antigen-presenting cells in the regulation of delayed-type hypersensitivity. II. Epidermal Langerhans' cells and peritoneal exudate macrophages. *Cell. Immunol.* **152,** 200–210
25. Komori, T., Doi, A., Furuta, H., Wakao, H., Nakao, N., Nakazato, M., Nanjo, K., Senba, E., and Morikawa, Y. (2010) Regulation of ghrelin signaling by a leptin-induced gene, negative regulatory element-binding protein, in the hypothalamic neurons. *J. Biol. Chem.* **285,** 37884–37894
26. Komori, T., Gyobu, H., Ueno, H., Kitamura, T., Senba, E., and Morikawa, Y. (2008) Expression of kin of irregular chiasm-like 3/mKirre in proprioceptive neurons of the dorsal root ganglia and its interaction with nephrin in muscle spindles. *J. Comp. Neurol.* **511,** 92–108
27. Lumeng, C. N., DelProposto, J. B., Westcott, D. J., and Saltiel, A. R. (2008) Phenotypic switching of adipose tissue macrophages with obesity is generated by spatiotemporal differences in macrophage subtypes. *Diabetes* **57,** 3239–3246
28. Komori, T., Morikawa, Y., Tamura, S., Doi, A., Nanjo, K., and Senba, E. (2005) Subcellular localization of glucose transporter 4 in the hypothalamic arcuate nucleus of ob/ob mice under basal conditions. *Brain Res.* **1049,** 34–42
29. Folch, J., Lees, M., and Sloane Stanley, G. H. (1957) A simple method for the isolation and purification of total lipides from animal tissues. *J. Biol. Chem.* **226,** 497–509
30. Taga, T., and Kishimoto, T. (1997) Gp130 and the interleukin-6 family of cytokines. *Annu. Rev. Immunol.* **15,** 797–819
31. Kamiya, A., Kinoshita, T., Ito, Y., Matsui, T., Morikawa, Y., Senba, E., Nakashima, K., Taga, T., Yoshida, K., Kishimoto, T., and Miyajima, A. (1999) Fetal liver development requires a paracrine action of oncostatin M through the gp130 signal transducer. *EMBO J.* **18,** 2127–2136
32. Morikawa, Y., Tamura, S., Minehata, K., Donovan, P. J., Miyajima, A., and Senba, E. (2004) Essential function of oncostatin m in nociceptive neurons

of dorsal root ganglia. *J. Neurosci.* **24,** 1941–1947
33. Mukouyama, Y., Hara, T., Xu, M., Tamura, K., Donovan, P. J., Kim, H., Kogo, H., Tsuji, K., Nakahata, T., and Miyajima, A. (1998) *In vitro* expansion of murine multipotential hematopoietic progenitors from the embryonic aorta-gonad-mesonephros region. *Immunity* **8,** 105–114
34. Wallenius, V., Wallenius, K., Ahrén, B., Rudling, M., Carlsten, H., Dickson, S. L., Ohlsson, C., and Jansson, J. O. (2002) Interleukin-6-deficient mice develop mature-onset obesity. *Nat. Med.* **8,** 75–79
35. Watt, M. J., Dzamko, N., Thomas, W. G., Rose-John, S., Ernst, M., Carling, D., Kemp, B. E., Febbraio, M. A., and Steinberg, G. R. (2006) CNTF reverses obesity-induced insulin resistance by activating skeletal muscle AMPK. *Nat. Med.* **12,** 541–548
36. Moreno-Aliaga, M. J., Pérez-Echarri, N., Marcos-Gómez, B., Larequi, E., Gil-Bea, F. J., Viollet, B., Gimenez, I., Martínez, J. A., Prieto, J., and Bustos, M. (2011) Cardiotrophin-1 is a key regulator of glucose and lipid metabolism. *Cell Metab.* **14,** 242–253
37. Stienstra, R., Joosten, L. A., Koenen, T., van Tits, B., van Diepen, J. A., van den Berg, S. A., Rensen, P. C., Voshol, P. J., Fantuzzi, G., Hijmans, A., Kersten, S., Müller, M., van den Berg, W. B., van Rooijen, N., Wabitsch, M., Kullberg, B. J., van der Meer, J. W., Kanneganti, T., Tack, C. J., and Netea, M. G. (2010) The inflammasome-mediated caspase-1 activation controls adipocyte differentiation and insulin sensitivity. *Cell Metab.* **12,** 593–605
38. Jager, J., Grémeaux, T., Cormont, M., Le Marchand-Brustel, Y., and Tanti, J. F. (2007) Interleukin-1β-induced insulin resistance in adipocytes through down-regulation of insulin receptor substrate-1 expression. *Endocrinology* **148,** 241–251
39. O'Rourke, R. W., White, A. E., Metcalf, M. D., Winters, B. R., Diggs, B. S., Zhu, X., and Marks, D. L. (2012) Systemic inflammation and insulin sensitivity in obese IFN-γ knockout mice. *Metabolism* **61,** 1152–1161
40. Grzelkowska-Kowalczyk, K., and Wieteska-Skrzeczyńska, W. (2010) Treatment with IFN-γ prevents insulin-dependent PKB, p70S6k phosphorylation and protein synthesis in mouse C2C12 myogenic cells. *Cell Biol. Int.* **34,** 117–124
41. Miyaoka, Y., Tanaka, M., Naiki, T., and Miyajima, A. (2006) Oncostatin M inhibits adipogenesis through the RAS/ERK and STAT5 signaling pathways. *J. Biol. Chem.* **281,** 37913–37920
42. Klover, P. J., Zimmers, T. A., Koniaris, L. G., and Mooney, R. A. (2003) Chronic exposure to interleukin-6 causes hepatic insulin resistance in mice. *Diabetes* **52,** 2784–2789
43. Senn, J. J., Klover, P. J., Nowak, I. A., Zimmers, T. A., Koniaris, L. G., Furlanetto, R. W., and Mooney, R. A. (2003) Suppressor of cytokine signaling-3 (SOCS-3), a potential mediator of interleukin-6-dependent insulin resistance in hepatocytes. *J. Biol. Chem.* **278,** 13740–13746
44. Matthews, V. B., Allen, T. L., Risis, S., Chan, M. H., Henstridge, D. C., Watson, N., Zaffino, L. A., Babb, J. R., Boon, J., Meikle, P. J., Jowett, J. B., Watt, M. J., Jansson, J. O., Bruce, C. R., and Febbraio, M. A. (2010) Interleukin-6-deficient mice develop hepatic inflammation and systemic insulin resistance. *Diabetologia* **53,** 2431–2441
45. Coll, A. P., Farooqi, I. S., and O'Rahilly, S. (2007) The hormonal control of food intake. *Cell* **129,** 251–262
46. Igaz, P., Salvi, R., Rey, J. P., Glauser, M., Pralong, F. P., and Gaillard, R. C. (2006) Effects of cytokines on gonadotropin-releasing hormone (GnRH) gene expression in primary hypothalamic neurons and in GnRH neurons immortalized conditionally. *Endocrinology* **147,** 1037–1043
47. Tamura, S., Morikawa, Y., Tanaka, M., Miyajima, A., and Senba E. (2002) Developmental expression pattern of oncostatin M receptor β in mice. *Mech. Dev.* **115,** 127–131
48. Odeleye, O. E., de Courten, M., Pettitt, D. J., and Ravussin, E. (1997) Fasting hyperinsulinemia is a predictor of increased body weight gain and obesity in Pima Indian children. *Diabetes* **46,** 1341–1345
49. Ishikawa, M., Pruneda, M. L., Adams-Huet, B., and Raskin, P. (1998) Obesity-independent hyperinsulinemia in nondiabetic first-degree relatives of individuals with type 2 diabetes. *Diabetes* **47,** 788–792
50. Mehran, A. E., Templeman, N. M., Brigidi, G. S., Lim, G. E., Chu, K. Y., Hu, X., Botezelli, J. D., Asadi, A., Hoffman, B. G., Kieffer, T. J., Bamji, S. X., Clee, S. M., and Johnson, J. D. (2012) Hyperinsulinemia drives diet-induced obesity independently of brain insulin production. *Cell Metab.* **16,** 723–737
51. Cho, H., Mu, J., Kim, J. K., Thorvaldsen, J. L., Chu, Q., Crenshaw, E. B., 3rd, Kaestner, K. H., Bartolomei, M. S., Shulman, G. I., and Birnbaum, M. J. (2001) Insulin resistance and a diabetes mellitus-like syndrome in mice lacking the protein kinase Akt2 (PKBβ). *Science* **292,** 1728–1731

Miyaoka and Miyajima *Cell Division* 2013, **8**:8
http://www.celldiv.com/content/8/1/8

CELL DIVISION

REVIEW Open Access

To divide or not to divide: revisiting liver regeneration

Yuichiro Miyaoka[2] and Atsushi Miyajima[1*]

Abstract

The liver has a remarkable capacity to regenerate. Even with surgical removal (partial hepatectomy) of 70% of liver mass, the remnant tissue grows to recover the original mass and functions. Liver regeneration after partial hepatectomy has been studied extensively since the 19th century, establishing the long-standing model that hepatocytes, which account for most of the liver weight, proliferate to recover the original mass of the liver. The basis of this model is the fact that almost all hepatocytes undergo S phase, as shown by the incorporation of radioactive nucleotides during liver regeneration. However, DNA replication does not necessarily indicate the execution of cell division, and a possible change in hepatocyte size is not considered in the model. In addition, as 15–30% of hepatocytes in adult liver are binuclear, the difference in nuclear number may affect the mode of cell division during regeneration. Thus, the traditional model seems to be oversimplified. Recently, we developed new techniques to investigate the process of liver regeneration, and revealed interesting features of hepatocytes. In this review, we first provide a historical overview of how the widely accepted model of liver regeneration was established and then discuss some overlooked observations together with our recent findings. Finally, we describe the revised model and perspectives on liver regeneration research.

Keywords: Akt, Cdks, Cellular hypertrophy, Cyclins, E2F family, Hepatocyte, Liver regeneration, mTOR, Partial hepatectomy, Polyploidy

Introduction

The liver has an extraordinary capacity to regenerate from various types of injuries [1,2]. The liver consists of various cell types, including hepatocytes, biliary epithelial cells, sinusoidal endothelial cells, stellate cells, and Kupffer cells; however, hepatocytes, which carry out most of the metabolic and synthetic functions of the liver, account for about 80% of liver weight and about 70% of all liver cells [3]. In severely damaged liver with impaired hepatocyte proliferation (in this review, the term "proliferation" means an increase in cell number due to cell division), facultative liver stem/progenitor cells, which have the potential to differentiate into both hepatocytes and biliary epithelial cells, proliferate and are assumed to contribute to regeneration [2,4,5]. In contrast, regeneration after surgical resection of a portion of the liver (partial hepatectomy, PHx) does not require such stem/progenitor cells; the remnant tissue undergoes hyperplasia to recover the original liver mass within about two weeks in rodents (Figure 1A and 1B) [6-9]. In fact, this process is not a true "regeneration" like that observed in limb or heart regeneration in newts [10]. The liver does not recover the original lobular structure; rather, the remnant tissue simply increases in size (Figure 1A). Although the term, "compensatory hyperplasia" more accurately describes this phenomenon, we use "liver regeneration" in this review, as it has been used widely. The multi-lobular structure of rodent liver allows the surgical resection of a lobe of choice to achieve different degrees of liver mass loss by PHx (Figure 1A) [1]. As the resection of lobes does not induce damage to the remaining liver tissue, PHx has long been considered an excellent experimental model for tissue regeneration.

The mention of liver regeneration by Prometheus in Greek mythology indicates that ancient people had noticed the regenerative capacity of the liver. Additionally, descriptions of liver regeneration can be traced back to the 19th century when liver mass restoration

* Correspondence: miyajima@iam.u-tokyo.ac.jp
[1]Laboratory of Cell Growth and Differentiation, Institute of Molecular and Cellular Biosciences, The University of Tokyo, Yayoi, Bunkyo-ku, Tokyo 113-0032, Japan
Full list of author information is available at the end of the article

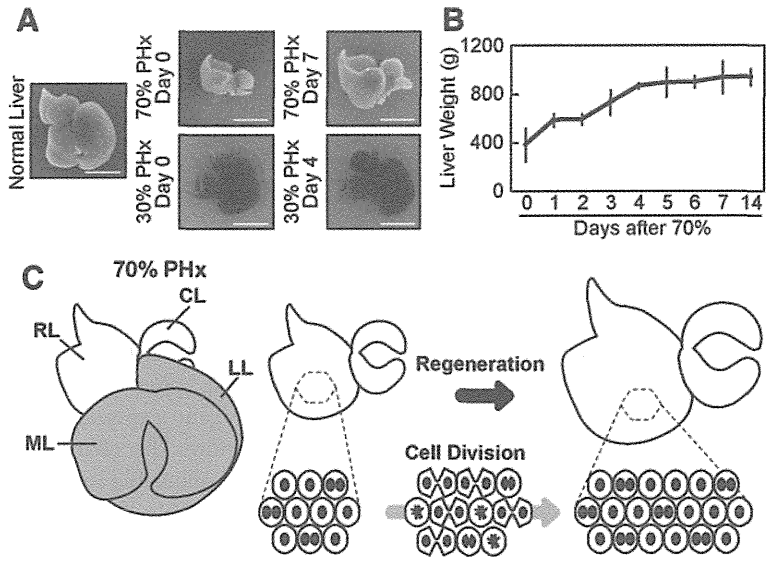

Figure 1 The widely accepted model of liver regeneration. (**A**) Liver regeneration. A normal mouse liver after 70 or 30% PHx (Day 0), and regenerated liver after 70 (Day 7) or 30% PHx (Day 4) are shown. Scale bars; 1 cm. (**B**) Liver weight change during liver regeneration after 70% PHx. The regeneration requires *circa* 14 days to recover the original liver weight. The error bars are S.D. (n = 3–7 for each day). (**C**) The currently accepted model of liver regeneration. In 70% PHx, the median lobe (ML) and the left lobe (LL) are removed, and the right lobe (RL) and caudate lobe (CL) regrow to restore the liver mass. In the traditional model, each hepatocyte is thought to divide once or twice during liver regeneration after 70% PHx. Potential alterations in size, nuclear number, and ploidy of hepatocytes are not taken into consideration.

with spontaneous healing of the scar was recognized after removal of a small portion of the liver [11]. In the early 20th century, it became possible to remove liver lobes by ligating blood vessels to reduce damage to the remnant liver tissue after surgery. In 1931, Higgins and Anderson carefully formulated the currently used procedure for PHx [12]. Notably, they used the term "liver restoration" instead of "liver regeneration" to distinguish clearly between compensatory hyperplasia and true tissue regeneration [12]. Since then, liver regeneration after PHx in rodents has been studied extensively for more than 80 years. Until the 1950s, liver regeneration was analyzed at mainly the tissue or cellular level by microscopic observations [13-15]. In the 1960s, the advent of electron microscopy enabled the analysis of hepatocyte ultrastructure in liver regeneration [16-19]. Almost at the same time, the epoch-making research tool of radioactive isotopes became available for biological studies. This technology was used to show that almost all hepatocytes incorporate radioactive nucleotides during liver regeneration after 70% PHx [20-25]. This landmark observation led to the establishment of the widely accepted concept that all remnant hepatocytes actively divide to recover the original cell number and liver mass (Figure 1C). This long-standing model postulated that all hepatocytes undergo roughly one or two rounds of cell division after 70% PHx [8,26,27].

Since the establishment of gene targeting technology in mice in 1989 [28-30], much effort has focused on identifying the genes required for liver regeneration. Many genes have been reported to be involved in liver regeneration after PHx [*e.g.*, β-catenin, methionine adenosyltransferase 1A (MAT1A), oncostatin M (OSM), nuclear factor (erythroid-derived 2)-like 2 (Nrf2) and c-Met] [31-35]. Most of these studies focused on the proliferation or survival of hepatocytes in accordance with the long-standing model. Although an elegant and simple model, accumulating evidence—including our recent findings—suggest that the traditional model of liver regeneration requires revision. We discuss these observations and the proposed revised model in the following sections.

Not all hepatocytes divide

The incorporation of radioactive nucleotides in hepatocytes during liver regeneration indicates that the cells entered S phase; however, this DNA replication does not necessarily mean that cell division occurred. If all hepatocytes undergo S phase and cell division after PHx, the ploidy should remain constant. However, it has long been known that hepatocyte ploidy is increased after PHx [14,36,37], suggesting that hepatocytes do not undergo conventional cell division. Previously, no convincing methods were available to investigate cell division in hepatocytes; however, we recently developed

a genetic tracing method to directly assess cell division using hydrodynamic tail vein injection (HTVi) for effective delivery of plasmids into hepatocytes [38-40]. In this way, we permanently labeled hepatocytes with LacZ by transiently expressing the Cre recombinase driven by the albumin promoter in hepatocytes in Rosa26-LacZ reporter mice (Figure 2A and 2B). By randomly labeling a small fraction of single hepatocytes, the fate of $LacZ^+$ hepatocytes after PHx could be precisely traced; *e.g.*, two neighboring $LacZ^+$ cells indicated that they were generated through one cell division, whereas single $LacZ^+$ cells indicated that no cell division occurred (Figure 2A and 2B). Recovery of the original mass after 70% PHx occurred over the course of two weeks (Figure 1B), and we counted the number of $LacZ^+$ cells during the regeneration. Surprisingly, no cell division was observed in more than 40% of hepatocytes, and the average number of cell divisions two weeks after 70% PHx was estimated as 0.7 times per hepatocyte, indicating that the number of hepatocytes increased by only 1.6-fold. Moreover, in the case of regeneration after 30% PHx (Figure 1A), hepatocytes did not undergo cell division, even though the original liver mass was recovered faster than that from 70% PHx. Interestingly, only a marginal fraction of hepatocytes entered into S phase after 30% PHx. Similar observations of infrequent S phase progression after 30% PHx were reported previously [14,41]. These observations indicate that hepatocyte proliferation alone does not account for liver regeneration after PHx.

Hepatocytes enlarge

The organ size is determined not only by the cell number, but also by the size of cells that constitute the organ [42]. Because the increase in hepatocyte number (1.6-fold increase) alone could not account for the increase in the liver weight (~2.4-fold increase after 70% PHx), we investigated hepatocyte size by imaging cytometry. We found that hepatocyte size increased significantly by 1.5-fold after both 30 and 70% PHx (Figure 3) [38]. This increase in cell size alone accounts for the increased liver weight after 30% PHx, explaining the observation that hepatocytes do not divide after 30% PHx. Moreover, a combination of increased cell size and hepatocyte number account for the increase in liver weight after 70% PHx ($1.5 \times 1.6 = 2.4$). Interestingly, increased hepatocyte size occurs as early as a few hours after 70% PHx, much earlier than their entry into the cell cycle, and peaks at 1 day after 70% PHx, suggesting that cell size increase is the first response of hepatocytes to the loss of liver mass. This very early stage of liver regeneration (0–4 hr after PHx in mice) is known as the "priming" phase, in which hepatocytes dramatically change their gene expression to prepare for regeneration [7,43]. Therefore, the change in transcriptional program seems to be responsible for the immediate hypertrophy of hepatocytes. Notably, the liver weight is almost unchanged from 1 day to 2 days after 70% PHx (Figure 1B). Because hepatocytes slightly decrease their size and start to actively enter the cell cycle from 1 day to 2 days after 70% PHx, this intervening time could be a period in which hepatocytes switch from a hypertrophic phase to a proliferative phase. The inhibition of cell cycle progression during liver regeneration has been shown to result in enlarged hepatocytes. Large hepatocytes in regenerated liver are observed in mice deficient for signal transducer and activator of transcription 3 (Stat3), S phase kinase-associated protein 2 (Skp2), separase or cyclin-dependent kinase 1 (Cdk1) [44-47]. Similarly, enlarged hepatocytes are observed in regenerating liver when the cell cycle in hepatocytes is blocked by dexamethasone [48]. However, our findings indicate that hypertrophy occurs in normal hepatocytes and precedes cell proliferation in liver regeneration. Importantly, the extent of hypertrophy is roughly the same in liver after 30 and 70% PHx, and hepatocytes do not divide after 30% PHx. Thus, hypertrophy is the first response in regeneration, and proliferation follows if hypertrophy is not sufficient to recover the original mass. In fact, Higgins

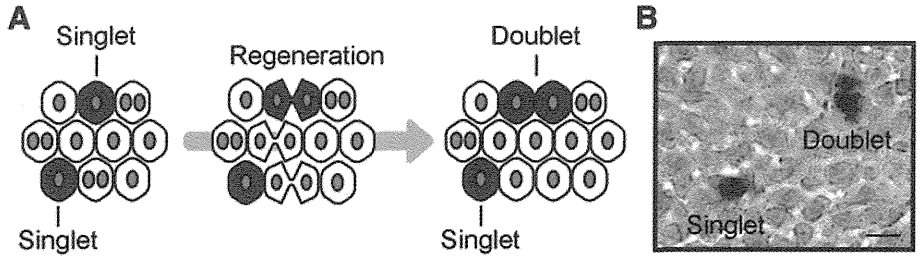

Figure 2 Single hepatocyte labeling assay for evaluation of hepatocyte division. (**A**) Schematic representation of the labeling assay. Using the optimized HTVi in Rosa26-LacZ mice, single hepatocytes (singlets) are genetically labeled by low-frequency expression of LacZ. A singlet that underwent a cell division cycle would result in a pair of neighboring labeled hepatocytes (doublet), whereas an undivided singlet would remain as a singlet. The frequency of cell division is estimated by counting the numbers of singlets and doublets. (**B**) A liver section showing a singlet and a doublet. A section of a regenerated liver with labeled hepatocytes after 70% PHx is shown. The pair of labeled hepatocytes is a doublet (upper), and the labeled hepatocyte (lower) is an example of a singlet. Scale bar; 25 μm.

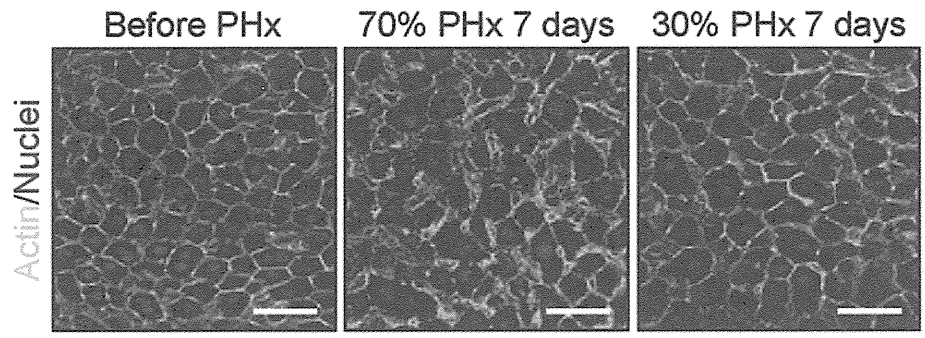

Figure 3 Hypertrophy of hepatocytes after PHx. Liver sections stained for actin (green) and nuclei (blue) are shown. The hepatocytes after 70 and 30% PHx are larger than those before PHx. Scale bars: 25 μm.

and Anderson mentioned in their 1931 report that hypertrophy of hepatocytes was the first response to the removal of liver tissue [12].

It is well known that hepatocytes accumulate massive amounts of lipids and glycogen immediately after 70% PHx [49-51]. Therefore, the rapid increase in hepatocyte size is at least partly due to lipid and glycogen accumulation. However, the lipid and glycogen amount decreases to normal levels by the completion of liver regeneration, and no obvious change in hepatocyte ultrastructure is observed in regenerated liver after 70% PHx, with the exception of enlarged nuclei [38]. Although several reports have shown that hepatocytes change the size and/or number of various organelles such as mitochondria, lysosomes, endoplasmic reticulum, and ribosomes [16-19,52], more studies are necessary to reveal the nature of cellular changes in regeneration. Although the detailed mechanism of hypertrophy requires further study, the Akt-mammalian target of rapamycin (mTOR) signaling axis, which regulates the size of various cell types [53], seems to be an important pathway for hypertrophy in liver regeneration. Akt is a serine-threonine protein kinase with pleiotropic functions such as regulation of cell growth, proliferation, survival, differentiation, and cytoskeletal changes. mTOR is another serine-threonine protein kinase directly phosphorylated by Akt and plays a central role in the functions of Akt. Akt is activated immediately after 30 and 70% PHx, and forced expression of an active form of Akt in hepatocytes increases their size [[44] and our unpublished data]. Another potential key player is c-Myc, which is a transcription factor involved in cell growth and cell cycle progression. Overexpression or deletion of c-Myc in hepatocytes increases or decreases their size, respectively [54-56]. Interestingly, both Akt-mTOR and c-Myc pathways play critical roles in the enhancement of protein synthesis, indicating that upregulation of gross protein synthesis is one mechanism underlying the hypertrophy of hepatocytes [54,57]. However, the upstream molecular mechanisms that sense the loss of liver tissue to activate Akt-mTOR and c-Myc pathways remain undefined (see below).

Because hepatocytes increase their size by 1.5-fold and then proliferate after 70% PHx, the 1.5-fold increase in cell size seems to be the threshold for hepatocytes to switch their response from hypertrophy to proliferation. As discussed above, this 1.5-fold size increase is sufficient to restore a 30% loss in liver mass, and hepatocytes do not proliferate after 30% PHx. Therefore, it would be interesting to determine precisely how much liver mass must be removed to induce proliferation. The molecular trigger for hepatocyte proliferation in liver regeneration is unknown. One possible explanation is that the size of the hepatocyte itself is the sensor to drive its cell division cycle, which is considered a general mechanism for activating cell division [58]. Further studies are required to address this question.

Hepatocytes infrequently enter M phase

Polyploidy is a characteristic feature in mammalian hepatocytes, and about 70% of adult hepatocytes in rodents are tetraploid [59]. In general, polyploid cells can arise from failed cytokinesis, mitotic slippage, cell fusion or endoreplication. Polyploid hepatocytes can be either mononuclear or binuclear. Polyploidization of hepatocytes is initiated in postnatal liver growth by incomplete cytokinesis, that produces binuclear polyploid hepatocytes, endoreplication that produces mononuclear polyploid hepatocytes, or both that produce binuclear polyploid hepatocytes [37,59,60]. Insulin signaling has been implicated in the polyploidization and binucleation at the weaning stage, as discussed below [37,60,61].

While it has long been known that ploidy of hepatocytes increases after PHx [14,36,37,62], its mechanism remains unknown. Although a majority of hepatocytes undergo S phase in regenerating liver after 70% PHx, not all hepatocytes undergo cell division, resulting in an increase in ploidy. We noticed that the ratio of hepatocytes that were positive for phosphorylated histone H3 (an M phase marker) to those that were positive for

Ki67 (a G1 to M phase marker) in liver regeneration is much lower than that in postnatal liver, where hepatocytes actively undergo cell division [38]. These results suggest that M phase progression is compromised in liver regeneration.

M phase promoting factor (MPF), composed of cyclin B and Cdk1, regulates entry into M phase [63,64], and MPF must be activated for cell transition from G2 to M phase. Cdk1 is phosphorylated at three amino acid residues (Thr-14, Tyr-15, and Thr-161) in the inactive form of MPF, whereas Cdk1 dephosphorylation at Thr-14 and Tyr-15 by cell division cycle 25 (Cdc25) activates MPF [65]. We found that the phosphorylation level of Cdk1 at Tyr-15 was much higher in regenerating liver compared to postnatal liver. Therefore, the lower activity of MPF in regenerating liver could be a cause of the infrequent entry into M phase. In fact, MPF activity is dispensable for liver regeneration; hepatocytes increase their size to regenerate liver after 70% PHx without cell division, even in the absence of Cdk1 [47].

In contrast to the G2 to M phase transition, the G1 to S phase transition is driven mainly by cyclin D/A2 and Cdk2 in normal cell division and endoreplication [66]. Therefore, it is intriguing to compare the activity of Cdk2 in liver regeneration with that in liver development. As hepatocytes increase their ploidy in both postnatal liver development and regeneration, the cell cycle regulators driving the G1 to S phase transition seem to dominate those driving the G2 to M phase transition in mature hepatocytes. Although the exact molecular mechanism that blocks the entry of hepatocytes into M phase in regenerating liver remains elusive, a crucial role of the E2F family transcription factors has been reported recently [67,68]. The E2F family consists of E2F transcription activators and transcription repressors and regulates cell cycle progression. Using mouse genetic models, these studies clearly showed that atypical E2F repressors E2F7 and E2F8 inhibit the completion of cell division to enhance polyploidy and binucleation in hepatocytes both in liver development and regeneration, whereas the canonical activator E2F1 counteracts their activities. These E2Fs differentially control the transcription of cell cycle regulators to either enhance or inhibit the G2 to M phase transition.

Cell division of binuclear hepatocytes to produce mononuclear cells

Binucleation is another interesting feature in adult hepatocytes that begins from the neonatal liver [60]. It has long been known that the number of binuclear hepatocytes decreases during liver regeneration after 70% PHx, as assessed by microscopic observations and manual counting [13-15,69-71]. Weaning increases the amount of circulating insulin to activate Akt signaling, which induces incomplete cytokinesis to generate binuclear hepatocytes during liver maturation [37,60,61]. In contrast, even though Akt is activated by PHx, the number of binuclear hepatocytes decreases in regenerating liver, suggesting that Akt has different functions in liver maturation and regeneration. Indeed, Akt signaling induces hypertrophy of hepatocytes in liver regeneration (our unpublished data). The different responses to Akt may be due to the molecular targets of the Akt signaling pathway differing according to the cellular context. mTOR is a major downstream molecule of Akt that functions in induction of hypertrophy. Because the E2F family transcription factors regulate the progression of M phase [67,68], it is tempting to speculate a link between Akt signaling and E2Fs in binucleation. Indeed, it is already known that this link exits in other cell types [72,73].

To elucidate the cellular basis underlying the reduction in nuclear number in liver regeneration, we investigated the behaviors of mononuclear and binuclear hepatocytes during liver regeneration using the genetic tracing method and observation of intracellular localization of Aurora B [38]. The intracellular localization of Aurora B differs among the M phase steps [74]; therefore, we could distinguish hepatocytes in prophase, prometaphase/metaphase, anaphase and telophase (Figure 4). We found that 32% of hepatocytes in prophase were binuclear, compared to only 1.9% of cells in prometaphase/metaphase. Furthermore, all hepatocytes in anaphase showed splitting of the two nuclei to their two poles, and 93% of pairs of daughter hepatocytes in telophase consisted of two mononuclear cells. Therefore, almost all cell divisions seemed to produce daughter mononuclear cells irrespective of the nuclear number of mother hepatocytes. Based on these observations, we speculate that mononuclear mother cells follow the normal cell division cycle, whereas binuclear mother cells gather their chromosomes at the center of the cells and split two nuclei to two daughter cells again. Consistently, the genetic tracing method showed that almost all pairs of neighboring daughter hepatocytes produced by cell division were pairs of two mononuclear hepatocytes [38]. Interestingly, this mode of cell division of binuclear hepatocytes was predicted from microscopic observations of hepatocytes in the early studies of liver regeneration [13,70]. Moreover, the same mode of cell division was later reported *in vitro* [75]. Our results reinforce this older prediction and suggest that this mode of cell division also occurs in binuclear hepatocytes *in vivo*. Although division of hepatocytes with multipolar spindles has been reported *in vitro* [76], further studies are required to address whether it also occurs *in vivo*.

Binucleation is generally considered a sign of terminal differentiation in both hepatocytes and cardiomyocytes [77,78]; however, in contrast to binuclear hepatocytes, binuclear cardiomyocytes do not divide. Mononuclear